Characterizing and dating authigenic phosphates from the sedimentary infill of Atapuerca archaeo-paleoanthropological cave sites (Spain)

I. Campaña[1*], M. Duval[2,3,4*], A. Álvaro-Gallo[2], V. Guilarte[5], Q. Shao[6], A.I. Ortega[7], L.J. Arnold[8], M. Demuro[8], J.M. Bermúdez de Castro[2], E. Carbonell[9,10]

[1] Departamento de Ecología y Geología, Facultad de Ciencias, Universidad de Málaga, Campo de Teatinos s/n, 29071 (Malaga, Spain)

[2] Centro Nacional de Investigación Sobre Evolución Humana (CENIEH), Paseo de la Sierra de Atapuerca 3, 09002 Burgos, Spain.

[3] Research Centre of Human Evolution, Environmental futures Research Institute, Griffith University, Nathan QLD 4111, Australia.

[4] Palaeoscience Labs, Dept. Archaeology and History, La Trobe University, Melbourne Campus, Bundoora, Victoria, Australia

[5] Departamento de Didáctica de las Ciencias Experimentales. Facultad de Ciencias de la Educación y del Deporte de Melilla, Universidad de Granada. Santander 1, 52005, Melilla, Spain

[6] School of Geography, Nanjing Normal University, Nanjing, 210023, China.

[7] Institución Fernán González. Real Adacemia Burgense de Historia y Bellas Artes. Pl. de España, 3 1ª. 09005 Burgos, Spain

[8] School of Physics, Chemistry and Earth Sciences, Environment Institute, and Institute for Photonics and Advanced Sensing (IPAS), University of Adelaide, North Terrace Campus, Adelaide, SA, 5005, Australia.

[9] IPHES, Institut Català de Paleoecología Humana i Evolució Social. C/ Marcelli Domingo s/n Campus Sescelades URV (Edifici W3). 43007 Tarragona, Spain.

[10] Universitat Rovira i Virgili (URV), Campus Catalunya, Avinguda de Catalunya 35, 43002 Tarragona, Spain.

***Corresponding authors**

Abstract

We present the results of a characterization and dating study of eight authigenic apatite samples collected from various stratigraphic units of three cave sites across the Atapuerca complex, namely Gran Dolina, Galería Complex and Sima del Elefante. Characterization analyses using X-ray diffraction, X-ray Fluorescence and Electron Spin Resonance (ESR) spectroscopy have been used to determine the nature and composition of the samples: seven of them are mostly made of hydroxyapatite, while one is composed of crandallite, and all show variable amounts of contamination by calcite and/or sediment. The timing of authigenic apatite formation, which results from the weathering of the limestone in a karstic environment, has been tentatively constrained through a combination of bulk and spatially resolved analyses using ESR and U-series methods. The dating results obtained enable the identification of various formation events during the Middle and Late Pleistocene at each site, around 170-180 ka and 110-120 ka in Gran Dolina, ~250 ka and ~40 ka in Galería Complex, and potentially ~360 ka in Sima del Elefante. Importantly, all these ages are significantly younger than the depositional age of the host sediment, thus confirming the post-depositional nature of authigenic apatite. Additionally, the absence of age consistency across sites suggests that they have all experienced independent diagenetic events, which cannot be attributed to the overall karst dynamics of the Sierra de Atapuerca, but should rather be regarded as local processes.

Beyond the dating results, this study provides an overview of the potential and current limitations of ESR and U-series methods applied to Quaternary authigenic apatite. The main complication regarding the ESR method lies in the evaluation of the internal dose rate given the high uranium concentrations measured in the samples, and the absence of a directly related alpha efficiency value for this type of material. Laser ablation U-series analyses also highlight the methodological challenges caused by significant spatial heterogeneity of the U-series data across the apatite samples, which reflects the complexity, non-uniformity and long duration of apatite formation processes around the limestone blocks.

Keywords: ESR dating, Atapuerca, Geochronology, Authigenic apatite, Uranium-series, Laser ablation, Diagenesis, Karst

1. Introduction

The Sierra de Atapuerca karst is widely known for its significant palaeoanthropological, archaeological, and palaeontological record, documenting an almost continuous human occupation from the Early Pleistocene to the Holocene (see an overview in Rodríguez et al., 2011 and references therein). The endokarstic system comprises three sub-horizontal levels (upper, middle, and lower) that are related to the fluvial terrace formation associated with the Arlanzón River (Ortega et al., 2013). The conducts of the middle endokarstic level opened to the outside during the Early Pleistocene, allowing for subsequent external sedimentary inputs, from the surface of the southwest flank of the Sierra de Atapuerca (Ortega et al., 2014; Benito-Calvo et al., 2017; Campaña et al., 2017), and for the possibility of human and animal presence. In the XIX century, the middle level was cut by a railway trench in the western area of the Sierra, leaving several karstic infills exposed, including the Gran Dolina-Penal group, Galería Complex, and Sima del Elefante (Ortega, 2009; Bermejo et al., 2017). While the rich archaeological and palaeontological record at these sites has triggered extensive multi-disciplinary research over the last few decades in order to gain a better understanding of past human occupations, other aspects of the sedimentary sequences have received much less attention. For example, this is the case with the authigenic apatite identified in various lithostratigraphic units of the three aforementioned railway trench sites (e.g., Pérez-González et al., 1995; Campaña, 2018; Campaña et al., 2022, 2023). In particular, the nature and chronology of these phosphate deposits have never been deeply investigated at Atapuerca, unlike in other regions of the Mediterranean (e.g. Greece, Levant; Karkanas et al., 1999; Weiner et al., 2002; Shahack-Gross et al. 2004).

The main goal of the present study is to characterize these common karstic minerals and to provide the first direct chronological constraint on their growth phases, in order to see whether they correspond to multiple formation events or to a single event that affected the middle level of the Sierra de Atapuerca endokarst system. To do so, we have employed the two main dating methods traditionally used on fossil teeth (e.g., Grün, 2009), whose main constituent is carbonated hydroxyapatite (Elliott, 2002): U-series and Electron Spin Resonance (ESR). The application of these dating techniques to authigenic apatite has rarely been investigated, despite the obvious similarities between this material and fossil tooth enamel in terms of mineralogical and chemical composition. However, it is worth mentioning the pioneering work by Rink et al. (2003) on the apatite veins in Tabun Cave (Israel), which demonstrated that non-biogenic apatite could be successfully dated using ESR. Consequently, the present study aims to provide an updated overview of the potential and current limitations of ESR and U-series methods applied to Quaternary authigenic apatite.

2. Authigenic apatite in karstic context: a brief overview

Phosphate deposits are commonly found in caves (e.g., Hill and Forti, 1997; Karkanas et al., 1999; Shahack-Gross et al., 2004; Onac, 2011) and are usually formed by the action of phosphate-rich waters reacting with limestone and precipitating stable minerals (Karkanas et al., 2000; 2002). The formation of phosphate minerals is a post-depositional process initiated by a source of phosphate (e.g., dissolved bones, bat guano or ashes; Karkanas et al., 2000) that provides an acid- and phosphate-rich environment. The phosphate-rich solutions react with existing minerals in the cave, leading to a sequence of transformations from more soluble to less soluble phosphate minerals: these include hydroxyapatite, crandallite, montgomeryite, taranakite and leucophosphite, which reflect increasing diagenetic intensity (Weiner et al., 2002).

Authigenic phosphates in caves have been extensively studied, especially in the Eastern Mediterranean, with a special focus on their formation mechanisms and archaeological implications. For example, investigations at Theopetra (Greece), Kebara and Hayonim (Israel) Caves showed that the formation of authigenic phosphate is closely related to a local source of phosphate, and therefore the occurrence of these minerals is usually restricted to well-defined areas of the sites (Karkanas et al., 1999; 2002; Schiegl et al., 1996; Stiner et al., 2001; Weiner et al., 1993). Further studies have focused on the diagenetic conditions under which the phosphate was formed, highlighting how the identification of authigenic minerals can help reconstruct past geochemical environments in cave sediments. In particular, the formation of these minerals depends on different chemical conditions, such as pH, temperature and elemental concentrations (Karkanas et al., 2000; 2002), therefore, authigenic phosphate mineral phases can indicate how these chemical conditions have changed in the past. The presence of phosphate minerals may also have taphonomic implications as it involves diagenetic processes that can partially or completely dissolve fossil remains and artefacts, especially bones (Karkanas et al., 2000), thereby impacting the preservation of the archaeo-paleontological record. Other studies have examined specific sources of phosphate in caves, such as guano deposits, which may provide a comprehensive understanding of the diagenetic processes occurring at a given site. The presence of guano accumulations on sediment surfaces has been identified as a primary trigger of chemical diagenesis, highlighting the central role of bat and bird colonies in shaping the diagenetic patterns within the caves (Shahack-Gross et al., 2004). It is also important to note that it is possible to identify the guano producer (for example birds, fruit bats, or insectivorous bats), which can be used to reconstruct different past environments, since these animals are sensitive to distinctive ambient conditions, such as open or closed cave system, temperature and humidity (Shahack-Gross et al., 2004; Friesem et al., 2021). For instance, a recent study has related the formation of phosphate crusts with archaeological animal penning areas (Polisca et al., 2025). These various examples

illustrate how the study of authigenic phosphate minerals may contribute to a better understanding of site formation processes, and indirectly provide crucial insights into the palaeoecology or even human activity (e.g. herding) at a site.

3. Atapuerca railway trench cave sites

3.1. Geological context

The three Railway Trench archaeological sites (Gran Dolina, Galería Complex and Sima del Elefante, from N to S; Fig. 1) all belong to the middle level of the endokarstic system of Sierra de Atapuerca (Ortega, 2009). This sinuous and sub-horizontal 500 m-long phreatic passage is found at an altitude of 1000-1003 meters above sea level (m.a.s.l.) and has been traditionally associated with the period of hydrological stability represented by terrace T3 of the Arlanzón River (+70-78 m) (Benito-Calvo et al., 2017; Ortega et al., 2013).

Gran Dolina site is a 25 m-thick cave sedimentary infill of Early to Middle Pleistocene sediments divided into 12 lithostratigraphic units (Campaña et al., 2017) (Figs. 1 and 2), named TD1-TD8, TD8-9, and TD9-TD11, from bottom to top. The sedimentary sequence may be divided into two main parts, the lowermost TD1 and TD2 units dominated by fluvial deposits (Campaña et al., 2022; Duval et al., 2022), and the overlying TD3 to TD11 units comprised of entrance sediments (gravity flow and fluvial facies) that document the opening of the cave (Campaña et al., 2017, 2022; Duval et al., 2022). These units are composed of alternating unconsolidated breccia of angular limestone clasts with reddish brown muddy matrix, well-sorted gravels, and yellowish red muddy layers. Among them, TD9 is made of phosphate-rich sediment that has been interpreted as a guano deposit (Parés and Pérez-González, 1999; Pérez-González et al., 2001; Vallverdú, 2002; Campaña et al., 2017). Another phosphate-rich layer is TD6.1.0, which contains hyena coprolites and is situated at the top of the TD6 unit (Campaña et al., 2016). In addition, phosphate crusts have been identified in various units of the sequence, namely TD4, TD5, TD6, TD8-9, TD9 and the lower part of TD10 (Campaña, 2018).

Galería Complex is situated south of Gran Dolina, and is composed of three sub-sections: Tres Simas, Galería, and Covacha de Los Zarpazos. The Galería sediments have been separated into five lithostratigraphic units named GI to GV from bottom to top (Figs. 1 and 2; Pérez-González et al., 2001, 1995). GI is a ~19 m-thick unit made of interior facies at the base of Galería Complex (Bermejo et al., 2017, 2020; Campaña et al., 2023). It is mainly composed of sand, silt and clay sediment with some speleothem growths. While the presence of crandallite has been identified in GI (Campaña et al., 2023), a white layer made of crandallite and hydroxyapatite especially stands out at the top of the unit. GII to GV units are dominated by entrance facies. They are composed by angular limestone

clasts with reddish brown muddy matrix deposits from the northern and the southern entrances, which are interstratified with gravels and muds in the middle area. In particular, the bat guano deposit within GII is interpreted as the origin of two black and white layers, where crandallite has been identified (Pérez-González et al., 1999, 1995; Falguères et al., 2013; Demuro et al., 2014). This guano layer reaches 20-30 cm thick in the southern and central parts of the section. These layers are related to the weathering of large clasts and fossil dissolution in the south of Galería, where post-depositional phosphate crusts were found (Falguères et al., 2013).

Sima del Elefante is a 25 m-thick cave sedimentary infill that has been divided into 16 litho-stratigraphic units called TE7 to TE21, from bottom to top (e.g., Rosas et al., 2001, 2006; Huguet et al., 2017). The sedimentary sequence is dominated by entrance facies deposits made of mudflows and debris flows (Figs. 1 and 2). These units are traditionally grouped into three sedimentary phases based on lithostratigraphic criteria: lower (TE7-TE14), middle (TE15-TE19), and upper (TE20-TE21) (Rosas et al., 2001, 2006). The lower phase is characterized by mudflows and gravity deposits with a pronounced dip that decreases towards the top. The middle phase is formed by waterlain sediments and a recurrent pattern of speleothem formation, with gravity sediments in the upper units. Finally, the upper phase is a short sequence that silted up the entrance of the cavity and was formed from debris fall and *terra rossa*. Up to four phosphate layers were identified within TE9 (lower phase). In particular, the presence of phosphate was observed within TE9c, one of the three sub-units of TE9, which are named c, b and a from bottom to top (Huguet et al., 2017). TE9c has two main sedimentary facies: yellow, red, brown, and black mud in laminated beds, where the phosphate layers were found, and stratified beds of gravelly mud (Huguet et al., 2017).

Fig. 1 approx here

3.2. Chronostratigraphic framework

A wide range of methods has been employed to chronologically constrain the sedimentary infill and associated fossil and archaeological record of the three Railway Trench archaeological sites, including luminescence (optically stimulated luminescence (OSL), thermally transferred optically stimulated luminescence (TT-OSL), thermoluminescence (TL) and post-infrared infrared stimulated luminescence (pIR-IRSL)), ESR (applied to quartz grains and fossil teeth), U-series, palaeomagnetism and biochronology (e.g., Álvarez-Posada et al., 2018 ; Arnold and Demuro, 2015; Arnold et al., 2015; Berger et al., 2008; Cuenca-Bescós & García, 2007; Cuenca-Bescos et al., 2015; 2016; Demuro et al., 2014, 2022; Duval et al., 2018, 2022; Falguères et al., 1999, 2013; Hernando et al., 2024; Moreno, 2011; Moreno et al., 2015; Parés and Perez-Gonzalez, 1995; Parés et al., 1999, 2006, 2013, 2018). This extensive geochronological work has produced an unprecedented dataset, but its interpretation is complicated by the age scatter that exists among some methods, in addition to

the fact that not all dating results may be regarded as equally reliable. While it is beyond the scope of the present work to critically evaluate the existing ages for these sites (for that purpose, see Parés et al., 2013; Falguères et al., 2013; Arnold et al., 2015 and Demuro et al., 2014), the individual chronostratigraphic framework available for each site may be summarized as follows.

At Gran Dolina, the Brunhes-Matuyama boundary (0.773 Ma; all geomagnetic boundaries are from Gradstein et al., 2020) has been identified within unit TD7 (Fig. 2). The lowermost stratigraphic units TD1 and TD2 have been constrained to between ~1.4 Ma and ~0.9 Ma (Duval et al., 2022) by a combination of electron spin resonance (ESR), single-grain thermally transferred optically stimulated luminescence (SG TT-OSL), and magnetostratigraphy. The overlying TD3-TD6 units are most likely constrained to ~0.9 Ma and 0.77 Ma (Álvarez-Posada et al., 2018; Duval et al., 2022), while TD6 has been dated to 0.85 ± 0.06 Ma using SG TT-OSL (Arnold et al., 2015), supported later by a direct combined U-series/ESR age on a *Homo antecessor* tooth (Duval et al., 2018). The upper part of the sedimentary infill has been constrained to between 610 ± 65 ka (TD8) and 337 ± 29 ka (TD10) by combined U-series/ESR dating of fossil teeth (Falguères et al., 1999; Parés et al., 2013), while younger luminescence ages (< 300 ka) have been proposed for the uppermost levels (Berger et al., 2008, but see Parés et al., 2013).

The general chronostratigraphy of Galería is perhaps comparatively more difficult to interpret given the existing age scatter (both for a given numerical dating method and among different methods). Focusing on the main section (Galería *sensu stricto*), a magnetic reversal tentatively correlated to the Brunhes-Matuyama boundary has been identified in the upper part of GI unit (Pérez-González et al., 2001), while SG TT-OSL dating from overlying sediment (GIb) in this section of Galería returned an age of 374 ± 33 ka (Demuro et al., 2014). The upper units GII to GIV have been constrained to between ~330 ka and ~250 ka using extended-range luminescence dating techniques (SG TT-OSL and pIR-IRSL$_{225}$), and between ~360 ka and ~200 ka with ESR/U-series dating method. A complete discussion of how these results compare with those from the other methods may be found in Falguères et al. (2013) and Demuro et al. (2014).

The sedimentary infill of Sima del Elefante may be divided into two main parts: the lower units TE7-TE16 showing reversed magnetic polarity and implying an age > 0.773 Ma (Parés et al., 2006), and the upper units (TE17-TE19) showing a normal polarity constrained to the Middle Pleistocene. The presence of the Brunhes-Matuyama boundary between TE17 and TE16 has been confirmed by SG TT-OSL and pIR-IRSL$_{225}$ dating of these two units to 724–781 ka and 804–864 ka, respectively (Arnold et al., 2015). A subsequent extended-range luminescence dating study using a combination of SG TT-OSL and pIR-IR$_{225}$ has additionally constrained layers TE18 and TE19 to 520-530 ka and ~240-290 ka, respectively (Demuro et al., 2022). The stratigraphically lowermost units TE9 and TE7

were initially numerically dated to ~1.1-1.2 Ma using the cosmogenic Al-Be burial method (Carbonell et al., 2008), while the revised ages recently proposed by Garba et al. (2024) remain within this range (although slightly younger).

Fig. 2 approx here

4. Material and Methods

4.1. Material

Eight apatite samples were collected from the Atapuerca Trinchera sites for characterization and dating purposes: three samples from Galería (ESR13-04, ESR13-05, and ESR13-06), four from Gran Dolina (ESR13-07, ESR13-08, ESR13-09, and ESR13-10) and one from Sima del Elefante (ESR13-11). A basic description and the stratigraphic location of the samples are provided in Table 1, Figs. 2 and 3. Additional sediment samples and limestone clasts were collected adjacent to the samples for the external dose rate reconstruction (Supplementary Fig. S1).

Fig. 3, Table 1 approx. here

4.2. Methods

4.2.1. Sample preparation

Phosphate samples were prepared and processed at the National Research Centre for Human Evolution (CENIEH; Burgos, Spain), following the standard ESR dating procedure traditionally used for fossil tooth enamel (e.g. Duval et al., 2011). Phosphate crusts were mechanically separated from the limestone clasts and then cleaned on both sides using a dentist drill to eliminate and minimize external alpha and beta contributions, respectively. The initial thickness and removed thickness on each side of the crust were measured. Clean phosphate crusts were then ground and sieved between 100 and 200 µm. Each powdered sample was subsequently split for subsequent characterization and dating analyses.

4.2.2. Characterization study

The mineralogical and chemical composition of the bulk phosphate samples were obtained by combining two techniques, X-ray diffraction (XRD) and wavelength dispersive X-ray fluorescence (XRF). Analyses were performed in the Archaeometry laboratory at CENIEH.

XRD was carried out using a PANalytical X'Pert PRO instrument equipped with a Cu target and a secondary monochromator. The operating conditions were 45kV/40mA in a continuous scan mode performed in the range of 2θ from 3° to 70°, with an increment of 0.02°. Samples were gently

grounded to a fine particle size to obtain powders suitable for XRD analysis. Mineralogical phase quantification was done with Rietveld refinement using the PANalytical software High Score Plus (Rietveld, 1969).

XRF was performed using a PANalytical Axios instrument. For each sample, 0.5 g of bulk material was ground and homogeneously mixed with 5 g of $LiBO_2$ / LiBr. The mix was then melted in a Pt-Au melting pot with a PANalytical Perl'X3 instrument. The following major oxides were measured: SiO_2, Al_2O_3, Fe_2O_3 total, MnO, MgO, CaO, Na_2O, K_2O, TiO_2, P_2O_5, and SO_3. Loss on ignition (LOI) was additionally calculated.

4.2.3. Dating study

4.2.3.1. Solution U-series analyses

Bulk solution U-series analyses were performed on a Neptune MC-ICPMS at Nanjing Normal University, China. The chemical protocol used for sample preparation was similar to that described in Douville et al. (2010). The uranium isotopes were measured using a peak jumping method by sequentially measuring ^{233}U, ^{234}U, ^{235}U, and ^{236}U on an ion counter, and ^{238}U in a Faraday cup. Thorium measurements were carried out immediately after uranium measurements for the same sample. The ^{229}Th and ^{230}Th isotopes were alternately measured on the secondary electron multiplier (SEM) and ^{232}Th was measured in a Faraday cup. Hydride interferences, machine abundance sensitivity and amplifier gains were evaluated every day prior to sample measurements. $^{230}Th/U$ ages were calculated by Monte-Carlo simulations (Shao et al., 2019) using half-lives of 75,584 years and 245,620 years for ^{230}Th and ^{234}U, respectively (Cheng et al., 2013).

4.2.3.2. Laser Ablation U-series analyses

ESR13-08 was selected for laser ablation (LA) U-series analysis. A cross section was extracted from the sample that had been previously embedded in epoxy resin. Analyses were carried out at the Research School of Earth Sciences, the Australian National University (Australia), using a custom-built laser sampling system interfaced between an ArF Excimer laser and a MC-ICP-MS Finnigan Neptune (for details, see Eggins et al., 2003, 2005), following the principles and procedures described in Grün et al. (2014). Five transects of 5-8 LA spots were performed across the sample (Fig. 4).

Fig. 4 approx here

4.2.3.3. D_E evaluation

The ESR dose evaluation was carried out at the ESR dating laboratory of the CENIEH, Spain, using a Multiple Aliquot Additive Dose (MAAD) procedure. Powdered samples were separated into ten aliquots. Nine of these aliquots were irradiated with a calibrated Gammacell 1000 ^{137}Cs gamma

source, using an almost double-spaced dose step distribution (Grün and Rhodes, 1991), while one aliquot was kept unirradiated (= natural aliquot). The following doses were given: 49, 98, 244, 586, 1074, 2148, 3850, 5572 and 9422 Gy.

ESR measurements were carried out at room temperature with an EMXmicro 6/1 Bruker ESR spectrometer coupled to a standard rectangular ER 4102ST cavity. To ensure constant experimental conditions over time, the temperature of the water circulating in the magnet was controlled and stabilized at 18 ºC by a water-cooled Thermo Scientific NESLAB ThermoFlex 3500 chiller, and the temperature of the room was kept constant at 20 ºC by an air conditioning unit. ESR measurements were performed with the following acquisition parameters: 1-20 scans, 2 mW microwave power, 1024-2048 points resolution, 15-75 mT sweep width, 100 kHz modulation frequency, 0.1 mT modulation amplitude, 60 ms conversion time, and 20 ms time constant depending on the samples and aliquots considered. For a given sample, the receiver gain value was optimized according to the ESR signal of the highest irradiated aliquot, and the same value was then used for all the aliquots from a given sample. In order to ensure similar resonance conditions in the ESR cavity for all the aliquots of a given sample, each aliquot was carefully weighed in the ESR tube, and a maximum variation of 1 mg in the mass was tolerated. Each aliquot of all samples (except ESR13-11, no rotation) was successively measured three times after rotating the tube in the cavity by about 120º. This procedure was repeated over three successive days without removing the phosphate powder from the ESR tubes between measurements in order to evaluate intensity and equivalent dose (D_E) repeatability. The ESR intensities were extracted from peak-to-peak measurement amplitudes of the apatite ESR signal (T1-B2) and then corrected by the corresponding receiver gain, number of scans, and aliquot mass. Baseline correction was not needed for most samples given their strong ESR signals. The only exception was ESR13-11, for which a baseline correction using a cubic function was employed. The ESR intensity of the high-frequency noise was evaluated from the high-field range domain of the ESR spectra obtained from the natural aliquot of each sample (e.g. Arnold et al., 2024). The signal-to-noise (S/N) value was calculated by dividing the ESR intensity of the radiation-induced signal (S) by that of the noise (N). An average S/N value was obtained from the three measurements performed on the natural aliquot rotations.

Fitting procedures were carried out with Microcal OriginPro 9.1 software using a Levenberg-Marquardt algorithm by chi-square minimization. Further details regarding the suitability of this algorithm for non-linear fitting may be found in Hayes et al. (1998). A single saturating exponential (SSE) function was fitted through the experimental data points and data were weighted by the inverse of the squared ESR intensity ($1/I^2$) (Duval and Grün, 2016). Final D_E values were obtained following the D_{max}/D_E criterion defined by Duval and Grün (2016), i.e. $5<D_{max}/D_E<10$ for D_E values <500 Gy,

$D_{max}/D_E \approx 5$ for D_E values between 500 Gy and 1000 Gy, and $0.9 < D_{max}/D_E < 1.8$ for D_E values >1000 Gy.

4.2.3.4. Dose rate evaluation and age calculation

To our knowledge, only one ESR dating study has previously focused on geological apatite (Rink et al., 2003). Given the rarity of this type of ESR dating application, there are no routine dating procedures or specific analytical programs available, and some assumptions have to be made based on our experience with fossil tooth enamel, which shares similarities with geological apatite. Indeed, fossil tooth enamel is almost exclusively made of biological hydroxyapatite (Elliot et al., 2002). Therefore, the ESR age estimates have been calculated with the DATA program (Grün, 2009), and using the following parameters: an alpha efficiency of 0.13 ± 0.02 (i.e., the value measured for tooth enamel; Grün and Katzenberger-Apel, 1994), Monte-Carlo beta attenuation factors from Marsh (1999), and dose-rate conversion factors from Adamiec and Aitken (1998). A density of 2.95 ± 0.20 g/cm^3 was assumed, i.e. similar to that usually considered for fossil tooth enamel. The cosmic dose rate was calculated according to Prescott and Hutton (1994).

Based on our observations in the field while collecting samples, and in the laboratory during sample preparation, most samples are composed of a > 1mm-thick crust (Table 1). Therefore, the geometry of each sample and its surrounding environment may be reasonably approximated to a succession of thin layers of varying thicknesses for beta dose rate evaluation (see Supplementary material Figure S2). U, Th and K concentrations in apatite, sediment and limestone blocks were determined by ICP-OES and ICP-MS analysis (Intertek Genalysis Laboratories) following a four acid digestion procedure. These elemental values were used to derive the internal, external beta and gamma dose rate components. An estimated long-term water content of 0 wt.% was assumed for the limestone block, and 20 ± 5 % (%wet weight) was assumed for the surrounding sediment, which is within range of long-term values usually employed for trapped-charge dating studies at Atapuerca (e.g., Demuro et al., 2014; Duval et al., 2018). When possible (e.g., for samples ESR13-05, ESR13-09 and ESR13-10), the gamma dose rate was derived from *in situ* measurements available from previous luminescence dating studies (i.e., Demuro et al., 2014 and unpublished data). These *in situ* measurements were carried out with a NaI probe connected to an Inspector 1000 multichannel analyser and processed following the 'windows method' to derive radioelement concentrations (Arnold et al., 2012). For samples with no *in situ* dosimetry available, the gamma dose rate was tentatively reconstructed using field observations and pictures taken from the outcrops. These pictures were rectified to decrease the deformation, and the area of each limestone clast identified in the surrounding matrix was measured using ArcGIS software. In this way, the ratio of clast vs sedimentary matrix was estimated, and assumed to be representative of the surrounding environment

of each sample within a 30 cm-radius sphere. This ratio was used to estimate the relative contribution of each material and to calculate the corresponding gamma dose rate for each of the ESR samples that lacked an associated in situ measurement.

ESR age calculations were carried out using the DATA program (Grün, 2009). Various uranium uptake models were tested, including two based on the combination of ESR and U-series data: the US model defined by Grün et al. (1988), and the CSUS model, which assumes rapid uranium uptake followed by a closure of the system (Grün, 2000). Finally, we also employed the Early Uptake (EU) model, i.e., a parametric model corresponding to a closed system assumption. Age uncertainties are given at 1σ throughout this study.

5. **Results**

5.1. Mineralogical and chemical analyses

Tables 2 and 3 list the mineralogical and chemical composition of the 8 samples. Except for ESR13-06, which is dominated by crandallite ($CaAl_3(PO_4)_2(OH)_5 \cdot (H_2O)$), all of the other samples are mainly composed of hydroxyapatite ($Ca_5(PO_4)_3(OH)$) (≥72 %). Among them, ESR13-04 is a pure phosphate sample (100 %). In comparison, ESR13-06 and ESR13-11 contains quartz (7-11 %) and phyllosilicate (9-10 %) minerals in their composition and are dominated by Fe, Si and Al elements, thus likely indicating non-negligible contamination by sediment. The other samples have variable amounts of calcite (from 3 to 23 %). The presence of calcite may be regarded as evidence for incomplete weathering of the limestone clast that sourced the phosphate (Karkanas et al., 2000). XRF chemical results are consistent with XRD analyses, but also indicate the presence of other minor minerals such as iron and manganese oxides. In particular, ESR13-06 (as well as ESR13-11 in a smaller proportion) shows higher Al content and lower Ca and P content than any other sample, which is consistent with the presence of crandallite and/or sediment in the samples.

Tables 2 & 3 approx. here

5.2. Solution U-series dating

U-series dating results are given in Table 4. Samples show uranium concentrations between 2.4 ppm (ESR13-04) and 38.8 ppm (ESR13-10), i.e. within the range of values that are typically measured in the dental tissues of fossil teeth from Atapuerca (previous studies by Falguères et al. (1999, 2013) have reported concentrations of between 0.2 and 5.5 ppm in the enamel, and 7-107 ppm in the dentine). While the lowest value corresponds to the pure hydroxyapatite sample, we do not observe any apparent correlation between the hydroxyapatite and uranium contents (see Tables 2 and 4).

Samples ESR13-06 and ESR13-11 show extremely high detrital Th content, several orders of magnitude higher than in the other samples, which is consistent with the mineralogical and chemical results that suggest the presence of sediment. Although these two samples show the lowest $^{230}Th/^{232}Th$ ratios, they are nevertheless >25, thus suggesting minimum impact (<5 ka) of detrital Th correction on the calculated U-series ages.

The U-series ages range from ~43 ka to ~253 ka for the samples from Galería, and from ~112 ka to ~180 ka for the samples from Gran Dolina. In contrast, ESR13-11 from Sima del Elefante returns the oldest age of the data set (~362 ka). Finally, ESR13-06 does not return a finite age, which indicates that the sample has experienced uranium leaching. This also indirectly shows that ESR13-06 does not behave as a closed system for U-series elements. However, this observation cannot necessarily be extrapolated to the other samples that yield apparent U-series age estimates, as only the combination of ESR and U-series data can enable meaningful evaluations of whether a given sample behaved as a closed system.

Table 4 approx. here

5.3. Laser Ablation U-series analyses

Five laser ablation (LA) tracks were performed across ESR13-08, systematically following the same direction from the inner limestone block to the outer part of the sample (Fig. 4). The resulting analytical data obtained for each individual LA spot are given in Supplementary Material Tables S1 to S5. A few additional LA spots were also performed in the epoxy resin for comparison, and no noticeable amounts of uranium and thorium were detected. The relatively large errors on the U-series results obtained from some laser ablation spots reflect the scatter of the data collected during the acquisition phase, and illustrates the local heterogeneity of the sample at the ablation spot.

The LA U-series data enable the identification of three main domains in ESR13-08, each with very distinct characteristics (Fig. 4). First, the inner limestone block is characterized by relatively low uranium concentrations (< 0.5 ppm), with no finite apparent U-series ages. This is consistent with the expected age of the limestone, which lies beyond the time range covered by the method (i.e., > 500 ka). In contrast, the authigenic apatite domain shows higher uranium concentrations of between 1 and 30 ppm, and apparent U-series ages ranging from ~77 ka and ~210 ka. Finally, the sediment yields uranium concentrations around 4-6 ppm and, as expected, much higher thorium contents (3-13 ppm) than any other domains (< 300 ppb, except for one LA spot).

Unlike bulk analyses, the spatially-resolved LA U-series analyses provide unprecedented insights into the authigenic apatite formation dynamics and the spatial heterogeneity of U-series elements. Under acid conditions, the authigenic apatite crystallizes at the interface between the phosphate-rich

sediment and the limestone block, while the latter is progressively being dissolved, thus providing the calcium carbonate that is necessary for the formation of the apatite (Karkanas et al., 2000; Onac & Forti, 2011; Audra et al., 2019). As a result, the dissolution/crystallisation front is expected to progressively migrate inwards, i.e. towards the centre of the limestone block. In other words, apparent U-series ages should theoretically show a progressive decrease from the outside to the inside of the block. This trend can be observed for several of the LA tracks. For example, LA track #3 shows an older age of ~212 ka on the outer part of the sample, while two younger and consistent ages of 120-130 ka (LA spots 4 and 5) are obtained towards the interior (Supplementary Material Table S3). In comparison, LA track #5 shows somewhat scattered results (e.g., LA spot 2 returns a much younger age of ~77 ka), but the outermost LA spot 5 yields the oldest apparent U-series age (~165 ka), while the innermost LA spot yields a younger age by several tens of ka (~128 ka) (Supplementary Material Table S5). In contrast, a couple of LA tracks show a different trend in apparent U-series age estimates through the cross-sectional profiles. For example, LA track #1 shows progressively younger results from the inner to the outer part of the sample, with LA spots 5 to 7 (Supplementary Material Table S1) returning ages from ~204 ka to 133 ka. A similar observation can be made for LA track #4, with two close ages of 160-170 ka from the inner side of the apatite, and two younger ages of 93-104 ka towards the outer part. While these older ages show large associated errors, possibly resulting in questionable reliability, we hypothesize that the results obtained from the inner part of the block probably reflect contamination by limestone (which returns U-series data close to or beyond equilibrium), as a result of incomplete dissolution. In other words, the various LA spots (namely, LA spot 5 of track #1, and LA spots 1 and 2 of track #4) are probably located in close proximity to the dissolution/crystallization front and incorporate a mixture of authigenic apatite and limestone, as indicated by the very low uranium concentrations measured (<2 ppm; Supplementary Material Table S1 and S4).

In summary, the spatially-resolved LA U-series data provide unique insights into the timing, duration and homogeneity of the apatite formation process. Based on the above, the ages obtained from the outer ring of the authigenic apatite may be regarded as the closest estimates for the beginning of the formation process. Apparent U-series ages from the outermost LA spots range from ~100 to ~212 ka depending on the area considered, which demonstrate that the authigenic apatite formation process is not uniform around the limestone block. Moreover, the progressive age change observed across the sample indicates that this is a continuous and progressive process that may last several tens of ka. Unfortunately, the spatial resolution of the present data set does not allow detailed interpretations regarding the authigenic apatite formation rate over time, and we cannot reasonably exclude that the crystallization results from a succession of periods with variable precipitation

intensity, including periods with no precipitation at all. Interestingly, many LA spots yield results that are between 120 and 140 ka, which is within close range to the age of ~118 ka given by solution U-series analysis on a bulk sample collected from ESR13-08 (Table 4), suggesting perhaps a phase of authigenic apatite formation around that time. The non-negligible age difference observed between two successive LA spots of a given transect (> 10 ka) also suggests that authigenic apatite precipitation may not be regarded as an even and continuous process. Finally, given the apparent relative inhomogeneity and porosity of the sample, we cannot exclude that the U-series ages are possibly impacted by local dissolution/recrystallization processes within the apatite.

5.4. ESR dating

5.4.1. ESR signals

An initial ESR acquisition was performed at room temperature using a large sweep width of 1000 G in order to visualize the various signals present in each natural sample (Fig. 5). Interestingly, the radiation-induced signal (RIS) created by CO_2^- radicals, which is usually observed in tooth enamel (e.g., Duval, 2015) and typically attributed to hydroxyapatite, is clearly visible in most samples (see red triangles in Fig. 5), the exception being ESR13-11. Another signal of unknown origin is also consistently visible on the left of the RIS in all samples (see blue triangles in Fig. 5). We were not able to identify this signal, which appears more or less visible among all samples depending on the intensity of the RIS. ESR13-05, ESR13-08 and ESR13-09 show an additional sextet (see orange triangles in Fig. 5) that may be related to the presence of calcite or limestone in the samples, as illustrated by the corresponding ESR spectra (Fig. 5). Both the calcite and limestone samples collected from Atapuerca display the typical lines attributed to the presence of Mn (e.g., Blanchard and Chasteen, 1976; White et al., 1977). Interestingly, these observations are confirmed by the XRD and XRF results. The three samples are composed of non-negligible proportions of calcite, which exceed 15% for ESR13-05 and ESR13-08 (Table 2). These two samples also show the highest Mn content (Table 3). In comparison, the analysis of ESR13-09 returns lower calcite and Mn contents, which is also clearly visible on the ESR spectrum, with the RIS showing an intensity >5 times higher than the Mn lines (Fig. 5). Specifically, we cannot exclude that the significant proportion of calcite observed in ESR13-05 and ESR13-08 may have a non-negligible impact on the T1-B2 ESR intensity measured for the RIS, and especially for the least irradiated aliquots, and thus on the D_E value that may be derived from these samples. While acknowledging the existence of this source of uncertainty, a more detailed discussion of its potential significance would be too speculative since its impact on the ESR results cannot be properly quantified here.

Fig. 5 approx. here

A second set of ESR acquisitions was performed on the natural samples using a smaller sweep width of 50-60 G in order to focus on the area around the RIS (Fig. 6). With the exception of ESR13-11, all samples show the RIS of hydroxyapatite with the usual T1, B1 and B2 peaks used for intensity evaluation (e.g., Grün, 2000). The absence of a visible RIS in ESR13-11, despite a relatively high hydroxyapatite content of 72 % (Table 2), is probably related to the non-negligible presence of sediment, as suggested by the XRD analytical results, which returned a compositional total of ~20% for quartz and phyllosilicate (Table 2). Additional interfering peaks can also be identified in the ESR spectra, including the line at 2.0057 (dark and light green triangles in Fig. 6) that is usually attributed to the SO_2^- signal (e.g., Grün, 2000). For some samples (ESR13-05, ESR13-08 and ESR13-09), this line (also called h-1 by some authors) correlates with calcite contamination (dark green triangles in Fig. 6), which is consistent with previous studies (e.g., Bahain et al., 1995; Martinez et al., 2001). A narrow line is also observed in the calcite reference sample, as well as in ESR13-05 and ESR13-08 (yellow triangles in Fig. 6), and may be tentatively related to a transient signal induced in calcite by grinding (Yokoyama et al., 1988). This signal was no longer visible in the ESR spectra acquired for dosimetry purpose about one year later.

Fig. 6 approx. here

5.4.2. D_E evaluation

After the first ESR acquisitions for signal characterization purposes, additional ESR measurements were performed following the standard analytical procedure for ESR dosimetry of tooth enamel (see details in section 5.3.3.). The average aliquot weight used for a given sample ranges from 22.2 to 58.7 mg (Table 5). The average S/N reported for each sample should be regarded as a minimum value, since it is based on the natural aliquot, which shows by definition the smallest radiation-induced ESR intensity of all aliquots for a given sample. All samples show an acceptable minimum S/N value ranging from 14.8 to > 100 (Table 5), indicating that the high-frequency noise has negligible, or no, impact on the ESR intensities and corresponding dose estimates measured from the radiation-induced signal. Repeated measurements show limited variability of the mean ESR intensities, which are $\leq$ 1 % for all samples, except ESR13-11 (4.3%) (Table 5). Resulting D_E values show high overall repeatability, with a variation of < 2% for 5 of 8 samples, and between 3.0 and 6.5% for the remaining three samples (Table 5). These values are within usual standards of those reported for tooth enamel (e.g., Duval et al., 2013). 6 of 8 samples show high goodness-of-fit (adjusted r^2>0.99; Table 5 and Fig. 7). In contrast, samples ESR1306 and ESR1311 show low goodness-of-fit with adjusted r^2 values of 0.94 and 0.88, respectively. This is visually confirmed by the existing scatter around the best fit observed in the dose response curves for the experimental points below 2000 Gy (Fig. 7). This scatter results in large relative D_E errors of 46 % and 68 %. Consequently, the reliability of the dose estimates

obtained for these two samples may be reasonably questioned. Interestingly, these are also the two samples with the lowest hydroxyapatite content (Table 2). For ESR13-11, the fitting issues may be explained by the difficulty of properly identifying and isolating the RIS for the least irradiated aliquots. There is a strong interfering signal (Fig. 5 and 6), which most likely affects the accuracy of the ESR intensity evaluation for the RIS. This is well illustrated by the large errors associated with the ESR intensities displayed on the DRC (Fig. 7).

Fig. 7 and Table 5 approx. here

5.4.3. Dose rate considerations and evaluation

The external dose rate evaluation requires an accurate determination of the nature, composition and radioactivity of the material surrounding each sample, i.e., within a ~30 cm and ~2 mm radius of the sample for the gamma dose rate and beta dose rate components, respectively. Hence, based on field and laboratory observations (Fig. 3 and Supplementary Material Fig. S1), the various elements composing the surrounding environment were thoroughly described for each sample (see schematic reconstructions in Supplementary Material Fig. S2) and various samples were collected within more or less close range of the samples for beta and gamma dose rate reconstruction.

5.4.3.1. Internal dose rate

ICP-MS/OES analytical results enable us to divide the apatite samples into different groups (Table 6). The first group includes ESR13-05, ESR13-07, ESR13-08, ESR13-09 and ESR13-10. These samples have similar low Th and K contents (<0.5 ppm and 0.05%, respectively) but much higher U-concentration values (>10 ppm). Given these results, the contributions of Th and K to the internal dose rate is minimal (≤ 1 % of the alpha dose rate for Th, the major component of the internal dose rate, and ~3-11% of the beta dose rate for Th+K). Group 2 is composed of samples ESR13-06 and ESR13-11. Both samples show significantly higher Th and K contents (>4 ppm and 0.5%, respectively; Table 6), which is consistent with the XRD results showing the presence of quartz and phyllosilicates and indicating sediment contamination (Table 2). As a consequence, the Th+K contribution to the internal dose rate is not negligible for this group of samples (4-19 % and 46-78 % of the alpha and beta components). Finally, ESR13-04 shows low U, Th and K contents (<0.5 ppm and <0.05%) and does not fit into either Group 1 or 2. This sample can be considered as intermediate between Group 1 and Group 2.

Table 6 approx. here

In summary, these results provide additional indications regarding the purity of the apatite samples and their suitability for ESR dating. Unlike Group 2 samples, ESR13-04 and the Group 1 samples have such low Th and K concentrations that their contributions to the internal dose rate would be

minimum and can therefore be reasonably neglected in the first instance, as is the case for tooth enamel samples, which are usually free of Th and K (Grün, 2009).

Finally, comparison of uranium concentrations derived from the solution ICP-MS elemental and U-series analyses shows some differences (see Tables 4 and 6), which are quite significant (>50%) depending on the sample considered. While we cannot exclude that these differences may partly reflect a bias in the laboratory procedures employed, they most likely illustrate the existing spatial heterogeneity in the samples, as illustrated by the spatially resolved LA U-series analyses (Tables S1 to S5). Since we have no evidence to question the reliability of either data set, we have calculated mean uranium concentration values for each sample and used these for the ESR age calculations.

5.4.3.2. External beta dose rate

For the purpose of external beta dose rate evaluation, the sample and its immediate surrounding (within ± 2 mm) were approximated as representing a succession of thin layers (Supplementary Material Fig. S2). 6 of 8 samples show the same geometry, with sediment on one side and limestone on the other side (see also Fig. 3). Both materials show a thickness > 2mm, indicating that they fully contribute to the external beta dose rate from each side. The other two samples, ESR13-06 and ESR13-11, are instead surrounded by sediment on both sides. Various samples of each component of the surrounding environment were collected (Supplementary Material Fig. S2) for ICP-MS/OES analyses in order to evaluate their natural radioactivity (Table 7).

All limestone samples return very low radioelement concentrations (U < 0.6 ppm, Th < 0.25 ppm, K < 0.025%) indicating that the external beta contribution from that side of the crust would be relatively small. Uranium concentrations are consistent with those independently obtained via LA analyses (Supplementary Material Tables S1 to S5). Moreover, this beta contribution is strongly attenuated by >95% given the magnitude of the initial and removed thicknesses for each sample, which exceed 3 mm and 80 µm, respectively (Table 8). The limestone clasts and sediment samples located closest to each apatite sample were selected for external beta dose rate evaluation (see summary in Supplementary Material Table S6; Table 8).

Table 7 approx. here

5.4.3.3.External gamma dose rate

Gamma dose rate values were calculated for three different scenarios (see summary in Supplementary Material Table S6). Scenario A is based on laboratory analysis and considers that the surrounding environment is composed of sediment only. These results should be regarded as maximum estimates since the environment also includes a non-negligible amount of limestone blocks with very low radioactivity. Therefore, the proportion of clasts and sedimentary matrix in the

surrounding environment was estimated from photographs, and assumed to be fairly representative of a 30-cm sphere around each sample. A new gamma dose rate evaluation was performed (scenario B), resulting in significantly lower estimates (by > 500 μGy/a) for most samples. Finally, a few samples have closely associated in situ measurements (scenario C). For example, ESR13-05 from GII layer (Galería site) may be correlated to luminescence sample ATG10-10 (Demuro et al., 2014). Samples ESR13-09 and ESR13-10 from Atapuerca Gran Dolina TD9 and TD10 can be associated with luminescence samples ATD14-2 and ATD14-1 (Demuro, pers. com.; unpublished results). The in situ values differ by about 10-30% from the laboratory-derived estimates, which illustrates the significant intrinsic uncertainty of the latter in highly heterogeneous sedimentary environments. By definition, laboratory gamma dose rate results are extremely sensitive to the clast/matrix ratio and this ratio cannot be properly evaluated from photographs and extrapolated to a 3D sphere. Regardless, the impact of those considerations is significantly reduced by the small weight of the gamma dose rate to the total dose rate (see discussion in section 7.1.). Age calculations were preferentially performed using gamma dose rates from in situ measurements (scenario C) when available (Table 8). Otherwise, a gamma dose rate evaluation based laboratory analyses (scenario B) was used (Table 8).

Table 8 approx. here

5.4.4. ESR age calculations

Considering the questionable ESR fitting results (Table 5) obtained for ESR13-06 and ESR13-11, as well as their U-series data being close to or beyond equilibrium (Table 4), and the limited purity of the apatite with non-negligible sediment contamination (Table 2), these two samples cannot be regarded as suitable for ESR dating. Consequently, no ESR age calculation was performed for them.

For the other six samples, combined U-series/ESR age calculations performed with DATA (see data inputs in Table 8) do not return any finite ages (Table 9), suggesting that the data inputs are close to or beyond the limits of the program. Additional calculations were carried out using the EU model (i.e., assuming a closed system), which yield late Middle to Late Pleistocene ages ranging from 197 ± 61 ka (ESR13-04) to 42 ± 4 ka (ESR13-05) (Table 9). The EU-ESR age is younger than the apparent U-series ages for 4 samples (Tables 4 and 9): ESR13-04 (EU-ESR: ~197 ka; U-series: ~253 ka), ESR13-07 (EU-ESR: ~54 ka; U-series: ~112 ka), ESR13-09 (EU-ESR: ~125 ka; U-series : ~180 ka) and ESR13-10 (EU-ESR: ~77 ka; U-series : ~171 ka). Such a pattern is usually interpreted as evidence for uranium leaching, suggesting that (i) the apparent U-series ages are most likely overestimated and (ii) the closed-system assumption based on the EU model is not met for these samples. Therefore, from a methodological point of view, the two data sets cannot be regarded as providing reliable chronological constraints. In contrast, the EU-ESR and apparent U-series ages are in agreement within error for the other three samples (ESR13-04: 197±61 ka (EU-ESR) and ~253 ka (U-series);

ESR13-05: ~42 ka and ~43 ka; ESR13-08: ~116 ka and ~118 ka), indicating that they behaved as closed systems for U-series elements. As a result, the numerical ages obtained for these samples may be regarded as reliable age constraints for the formation of the apatite.

Table 9 approx. here

6. Discussion

6.1. Methodological considerations

Given the restricted number of ESR dating studies based on geological apatite, our general knowledge and understanding of this specific geochronological application remains limited (i.e., in contrast to ESR dating of fossil tooth enamel, or optically bleached quartz grains; e.g., Duval et al., 2020). As such, the present work may be regarded as experimental from a methodological point of view. In particular, we acknowledge that the ESR, U-series, or any associated data collected from the apatite samples, and their combination for dating purpose, may naturally raise a series of questions around the robustness and the reliability of the results, and can help to identify the main sources of uncertainty in the dating procedure.

In the first instance, the ESR dating results indicate that many apatite samples do not behave as a closed system for U-series elements. In other words, the closed system assumption should not be systematically taken for granted for authigenic apatite. When considering all samples, the total dose rate is largely dominated by the internal component (Table 9), whose weighting ranges from about 60 % (ESR13-04) to 91 % (ESR13-09 and ESR13-10) of the total dose rate. This internal component is dominated by the alpha dose rate with relative contribution of 58-68 % depending on the sample considered, which is consistent with previous observations by Rink et al. (2003). As a consequence, the external dose rate, and especially the gamma dose rate, carry very limited weight on the total dose rate calculation (<20% for all but one sample – ESR13-04, ~34 %), thus minimizing any existing uncertainty around its evaluation, as discussed above (section 5.4.3.3.).

The overall uncertainty of the ESR dating results is therefore most likely driven by the internal dose rate. Given its magnitude (4000-10500 µGy/a; Table 9) and its resultant weight on the total dose rate, we cannot reasonably exclude that it might be significantly overestimated. This may be indirectly confirmed by the ESR age calculation attempts using the CSUS model: even when considering a rapid uranium uptake scenario, the modelled internal dose value calculated for several samples (ESR13-07, ESR13-08 and ESR13-09; Table 9) is higher than the experimental D_E value, leaving no possibility for incorporating the external dose rate into the finite age calculation. This demonstrates that the ESR and U-series data are not compatible, and supports the hypothesis of a significant overestimation of the internal dose rate.

Three main parameters significantly impact the evaluation of the internal dose rate: uranium concentration, apparent U-series age and alpha efficiency. Our spatially resolved LA U-series data collected for ESR13-08 show that the solution U-series analytical results might be biased by significant spatial heterogeneity of radioelements, with some domains within the apatite samples locally showing significantly higher uranium concentrations, and others being contaminated by incompletely dissolved limestone, whose U-series data are at secular equilibrium. The latter is consistent with the independent observations derived from the XRD (Table 2) and ESR data (Figs. 7 and 8). Both situations (higher uranium concentration or older apparent U-series age) would have a similar influence on the dose rate evaluation, leading to the calculation of a higher internal dose rate. In a similar way, the impact of dentine contamination in the enamel has also been observed in other studies (e.g., Duval et al., 2018). Moreover, like Rink et al. (2003), we used the alpha efficiency value traditionally employed for tooth enamel (0.13; Grün and Katzenberger-Apel, 1994), but we acknowledge that its accuracy for geological apatite is currently unknown. Additionally, several ESR studies based on fossil teeth (e.g., Bahain et al., 1992; Duval et al., 2012) have showed the difficulty of dating samples with high uranium concentration in the enamel (> 2 ppm). For this reason, it has been hypothesized (although not confirmed by experimental data so far) that there might be an inverse correlation between the alpha efficiency and the uranium concentration. In other words, higher concentrations would naturally lead to an increased trap or signal destruction, and thus a decrease of the alpha efficiency. In the present study, relatively high uranium concentrations were measured in most (5/6) samples (14-37 ppm; Table 8), thus leading to the calculation of very large internal dose rates (Table 9). Consequently, following the conclusions drawn for fossil tooth enamel, we cannot reasonably exclude that this component may be overestimated. Basic sensitivity tests using an alpha efficiency divided by 2 (e.g., 0.07) for samples showing high uranium concentrations (i.e., all samples except ESR13-04) return older EU-ESR ages by between +11 ka (ESR13-05) and + 60 ka (ESR13-09). This impact is limited by the fact that the alpha dose rate represents about 60% of the internal dose rate, with the other 40% corresponding to the beta component. In contrast, CSUS-ESR age estimates are older by a factor >2 for three samples when using an alpha efficiency divided by 2, whereas no result can be obtained for ESR13-07 and ESR13-10, suggesting that an internal dose rate overestimation can only be partly explained by the use of an inappropriate alpha efficiency value.

To sum up, there is a non-negligible uncertainty on the alpha efficiency, as well as on the spatial homogeneity of the U-series data, which could possibly induce a significant internal dose rate overestimation. Finally, it should also be kept in mind that the LA U-series data suggest that apatite formation may not be regarded as an immediate process, but rather takes several tens of ka. This may have significant implications and add complexity as far as internal dose rate evaluation, as well as

introduce strong time dependency for some parameters like the alpha and beta self-absorption factors. All of the above considerations illustrate the experimental aspect of this work and the difficulty of dating this kind of deposits using the ESR method. Accordingly, we cannot exclude that the apparent discrepancy between the EU-ESR and U-series ages observed earlier and the possible occurrence of uranium leaching could simply be artificially induced by an internal dose rate overestimation. In other words, we cannot reasonably exclude that the apparent U-series ages may be reliable age constraints. This possibility is taken into account in the following discussion.

6.2. Constraining the age of apatite formation in Atapuerca

6.2.1. Gran Dolina

As explained above, the existing ESR and U-series data sets obtained for the four samples collected from Gran Dolina may be interpreted in two different ways. On the one hand, the combination of ESR and U-series data suggests that among these samples, only one (ESR13-08) behaved as a closed system for U-series elements, while the others may have experienced uranium leaching. Therefore, the reliability of the apparent U-series ages obtained for samples ESR13-07, ESR13-09 and ESR13-10 may be questioned. In this context, the age of ~120 ka obtained for ESR13-08 by two independent methods (EU-ESR and U-series), which is also compatible with the LA U-series data, is the only reliable constraint for the formation of the apatite. On the other hand, it cannot be excluded that the apparent discrepancy observed between ESR and U-series data might simply result from the existing uncertainty around the dose rate evaluation (see section 6.1.), and in particular a potentially overestimated internal dose rate. In this context, the apparent U-series ages may be regarded as reliable age constraints, and they suggest the occurrence of two apatite formation events: one around 170-180 ka in the upper units TD9 (ESR13-09) and TD10 (ESR13-10), and another later, around 110-120 ka for the lower TD4 (ESR13-07) and TD6 (ESR13-08) units. Importantly, these results are significantly younger than, and therefore compatible with, the known depositional age obtained for these various units, confirming the post-depositional formation of authigenic apatite in Gran Dolina.

Our data lead to the secure identification of at least one apatite formation event affecting TD6 and dated to ~120 ka, i.e., post-dating by about 720 ka the depositional age of the sediment dated to 0.85 ± 0.06 Ma (Arnold et al., 2015). When considering all chronological, stratigraphic and sedimentological evidence available, the following interpretation may be proposed. First, the phosphate crusts in Gran Dolina are situated in the SE of the section, and they seem to be related to a cut-and-fill that starts in TD9 and reaches TD4 (Pérez-González et al., 2001). TD9 has been initially described as a narrow phosphatic layer most likely resulting from the accumulation of bat guano (Pérez-González et al., 2001; Campaña et al., 2017). It may be regarded as the most probable source of phosphate in Gran Dolina, which is consistent with the oldest apparent U-series age obtained for

ESR13-09, suggesting an early weathering event in TD9. This event most likely also impacted the stratigraphically overlying unit TD10 unit, which may be explained by the geometry of the deposits. Phosphate crusts identified within TD10.4 are indeed mainly located in the SE section that is topographically positioned below TD9 in the northwest (Campaña et al., 2017). Therefore, phosphate migration from TD9 to TD10 is plausible, supporting thus TD9's bat guano as the source of phosphate. A second event of apatite formation within TD6 and TD4 may be identified, about 60-70 ka later than the first event identified in TD9-TD10. The source of the phosphate for this second event could be the hyena coprolite accumulation at the top of the TD6 unit (TD6.1.0 layer), which is formed by phosphates (Campaña et al., 2016; Pineda et al., 2017). This accumulation is situated in the southeast of the stratigraphic section. Nevertheless, the results of LA U-series (Supplementary Material Tables S1 to S5) also indicate that the formation of the phosphate crust in TD6 may have started earlier, at a similar time to the event recorded in TD9-TD10, and lasted for several tens of ka. The thickness of the phosphate crusts in TD6 also suggests a longer formation time than in other layers.

6.2.2. Galería

Three samples were collected from Galería site (ESR13-04, ESR13-05, ESR13-06). Among them, the internally consistent EU-ESR and U-series ages estimates obtained for ESR13-04 and ESR13-05 indicate they both behave as closed systems. Although they both belong to the same stratigraphic Unit GII dated to 242 ± 17 ka by luminescence (Demuro et al., 2014) and 350-363 ka by ESR/U-series (Falguères et al., 2013), they return significantly different ages (Table 9), suggesting that Unit GII has experienced at least two different phases of apatite formation. The numerical age of ~250 ka obtained for ESR13-04 indicates that a first phase of apatite formation occurred very close in time to sediment deposition, whereas a second phase may be documented later, about 40 ka. No reliable age constraint could be obtained through either ESR and/or U-series for ESR13-06 from Unit GI. In particular, U-series data beyond secular equilibrium indicate that the sample has experienced uranium leaching. The timing of this formation event therefore cannot be constrained with the present data set.

In Galería, phosphate crusts are only found inside and below the black and white layers of GII unit, which are interpreted as bat guano (Pérez-González et al., 1999, 1995; Falguères et al., 2013; Demuro et al., 2014). These layers are the only possible phosphate source identified in the site. While it may be hypothesized that authigenic apatite formation in GII and GI results from the leaching of the phosphate from the bat guano and its subsequent precipitation in the underlying layers, this cannot be confirmed by the present data set given the absence of reliable age constraint for the sample from GI. Interestingly, the two phases of apatite formation dated to ~250 ka and ~40 ka cannot be correlated to the precipitation events identified in Gran Dolina. This suggests that both sites have experienced

independent diagenetic events, which cannot be attributed to the overall karst dynamics of the Sierra de Atapuerca, but should rather be regarded as local processes.

6.2.3. Sima del Elefante

In Sima del Elefante, phosphates are only found in the human fossil-bearing deposits of TE9c sub-unit (Carbonell et al., 2008; Huguet et al., 2017), within three 5 cm thick layers of unconsolidated greyish brown silts. The only chronological constraint available for sample ESR13-11 is the apparent U-series age estimate of ~360 ka (Table 9), which should be treated with caution since its reliability cannot be properly evaluated. This chronology is nevertheless compatible with the older depositional age of 1.1-1.2 Ma (Carbonell et al., 2008; Garba et al., 2024) established for TE9 through cosmogenic nuclides burial dating. The very localized presence of phosphates in Sima del Elefante site suggests that acid events were more limited at this site than in Gran Dolina and Galería. Although the source of the phosphate is uncertain, the lithology of TE9c is similar to that of the TD8-9 and TD9 deposits of the Gran Dolina (Huguet et al., 2017), suggesting that this level may have had some input of bat guano.

6.3. Additional considerations regarding the fossil and archaeological record

Two phosphate samples were taken from key human fossil-bearing units, ESR13-08 from TD6.2 (Gran Dolina) and ESR13-11 from TE9c (Sima del Elefante). The presence of phosphates in these units indicates weathering events in the sediment that could possibly affect the preservation of fossil remains (Karkanas et al., 2017). Bone dissolution may start in sediments with a pH <8.1 (Berna et al., 2004), with increasing intensity below 7 (Hedges and Millard, 1995). The hydroxyapatite forming phosphate crusts is stable at a pH between 8 and 7, while crandallite and montgomeryite form at pH < 7 (Karkanas et al., 2000). The absence of the latter two minerals in TD6.2 and TE9c indirectly indicates that the pH did not go below 7 and therefore bone dissolution, if any, has been most likely very limited. This is confirmed by the absence of weathering features observed on the human teeth from TE9c, as well as by the presence of a noticeable small mammal fossil record (Carbonell et al., 2008). Additionally, despite the identification of many phosphate crusts within the fossil-rich TD6.2 sub-unit hosting *Homo antecessor* remains in the southeast wall of the vertical pit (Bermúdez de Castro et al., 2017 and references therein), spatial analysis indicates that there is no significant lateral variation in the number of fossil remains (Campaña et al., 2016), nor weathering features in the fossil remains (Saladié et al., 2021) near the south-east wall of the vertical pit. This indicates that, despite the pH being below 8 at the time of phosphate crust formation, the pH most likely remained closer to 8 than 7 in this area (Karkanas et al., 2017), thus limiting any significant impact on fossil preservation. Instead, the crandallite found in units GI and GII at Galería (Pérez-González et al., 1995; Demuro et al., 2014; Campaña et al., 2023) indicates that the pH was possibly below 7. Given these conditions,

significant fossil dissolution processes are expected for GII where crandallite was identified in the white layers, unlike for GI, which is formed by cave interior facies that are palaeontologically sterile (Rodríguez et al., 2011; Campaña et al., 2023). In contrast, TD9 has been described as an archaeologically sterile unit (Fernández-Jalvo, 1995; Blain et al., 2009). Despite the absence of crandallite in this unit (Table 2), which would indicate that the pH was consistently above 7, no fossil remains were discovered. This suggests that the fossilized material was possibly dissolved, which could have been caused by the bat guano deposit that forms this unit and would provide a stable acid environment for a long period. Finally, the pH conditions documented by the phosphate-bearing layers is not expected to significantly impact the preservation of lithic tools based on flint, quartzite and quartz, whose solubility threshold has been defined above a pH of 8.0-8.5 (Krauskopf, 1979).

7. Conclusion

The presence of authigenic apatite, formed by the weathering of limestone in karstic environments, has received little attention so far Atapuerca, although it documents the existence of intense post-depositional processes occurring in the sedimentary infill, i.e. long after the sediment deposited. Through a characterization and dating study of geological authigenic apatite collected from various stratigraphic units and cave sites across the Atapuerca complex, the present work contributes to improve our understanding of processes that occurred throughout the Middle and Late Pleistocene. Interestingly, our dating results indicate that the sites have all experienced independent diagenetic events, which cannot be attributed to the overall karst dynamics of the Sierra de Atapuerca, but should rather be regarded as local processes. From a methodological point of view, the results obtained here show the potential and current limitations of the ESR and U-series dating methods applied to geological apatite, and help to identify future avenues worth exploring in order to improve authigenic apatite dating reliability and accuracy. In particular, any further dating attempts will specifically require proper evaluation of the alpha efficiency for this type of material, which currently appears to be one of the main sources of uncertainty affecting the combined U-series/ESR dating results.

Acknowledgments

Aspects of this study have been supported by an Australian Research Council Future Fellowship Grant (FT150100215) and a Ramón y Cajal fellowship (RYC2018-025221-I) granted to M. Duval. The latter is funded by MCIN/AEI/10.13039/501100011033 and by ‘‘ESF Investing in your future”. This work is also part of Grants PID2021-123092NB-C21/-C22 and PID2021-122355NB-C33 MCIN/AEI/ 10.13039/501100011033/’ERDF A way of making Europe’. I. Campaña is the beneficiary recipient of a post-doctoral grant fellowship from Junta de Andalucía. The U-series

analysis of Qingfeng Shao was supported by National Key R&D Program of China (2023YFF0905700). We would like to express our sincere gratitude to the current and past coordinators of the archaeological excavations at Gran Dolina, Galería Complex and Sima del Elefante sites for their invaluable help while this work was carried out (in alphabetic order): Isabel Cáceres, Antoni Canals, Paula García-Medrano, Rosa Huguet, María Martinón-Torres, Marina Mosquera, Andreu Ollé, Xosé Pedro Rodríguez-Álvarez, Jordi Rosell, Palmira Saladié, Elena Santos and Josep Vallverdú. We also thank the Atapuerca Research Team (EIA) and the Fundación Atapuerca for continuous support over the last decade. Part of the laboratory analyses was carried out at CENIEH-ICTS with the support of the CENIEH staff. This work has benefited from discussions with Lucía Bermejo Albarrán, Alfonso Benito-Calvo and Josep M. Parés.

References

Adamiec, G., Aitken, M. J., 1998. Dose-Rate Conversion Factors: Update. Ancient TL 16(2), 37-50.

Álvarez-Posada, C., Parés, J.M., Cuenca-Bescós, G., Van der Made, J., Rosell, J., Bermúdez de Castro, J.M., Carbonell, E., 20218. A post-Jaramillo age for the artefact-bearing layer TD4 (Gran Dolina, Atapuerca): New paleomagnetic evidence, Quat. Geochr. 45, 1-8. doi: 10.1016/j.quageo.2018.01.003.

Arnold, L.J., Demuro, M., 2015. Insights into TT-OSL signal stability from single-grain analyses of known-age deposits at Atapuerca, Spain. Quat. Geochr. 30B, 472-478.

Arnold, L.J., Duval, M., Falguères, C., Bahain, J.-J., Demuro, M., 2012. Portable gamma spectrometry with cerium-doped lanthanum bromide scintillators: Suitability assessments for luminescence and electron spin resonance dating applications. Radiation Measurements 47(1), 6-18.

Arnold, L.J., Demuro, M., Parés, J.M., Pérez-González, A., Arsuaga, J.L., Bermúdez de Castro, J.M., Carbonell, E., 2015. Evaluating the suitability of extended-range luminescence dating techniques over Early and Middle Pleistocene timescales: Published datasets and case studies from Atapuerca, Spain. Quaternary International 389, 167-190.

Arnold, L.J., Demuro, M., Duval, M., Grün, R., Sanz, M., Costa, A.M., Araújo, A.C., Daura, J., 2024. Single-grain luminescence and combined U-series/ESR dating of the early Upper Palaeolithic Lagar Velho Rock Shelter, Leiria, Portugal. Qua. Geochr. 83, 101572.

Audra, P., De Waele, J., Bentaleb, I., Chroňáková, A., Krištůfek, V., D'Angeli, I. M., Carbone, C., Madonia, G., Vattano, M., Scopelliti, G., Cailhol, D., Vanara, N., Temovski, M., Bigot, J.-Y., Nobécourt, J.-C., Galli, E., Rull, F., Sanz-Arranz, A., 2019. Guano-related phosphate-rich minerals in European caves. Int. J. of Speleo. 48(1), 75-105.

Bahain, J.-J., Yokoyama, Y., Falguères, C., Bibron, R., 1995. Datation par resonance de spin electronique (ESR) de carbonates marins quaternaires (Coraux et coquilles de mollusques). Quaternarie 6(1), 13-19.

Bahain, J.-J., Yokoyama, Y., Falguères, C., Sarcia, M.N., 1992. ESR dating of tooth enamel: a comparison with K-Ar dating. Quaternary Science Reviews 11, 245-250.

Benito-Calvo, A., Ortega, A.I., Pérez-González, A., Campaña, I., Bermúdez de Castro, J.M., Carbonell, E., 2017. Palaeogeographical reconstruction of the Sierra de Atapuerca Pleistocene sites (Burgos, Spain). Quat. Int. 433, 379–392. https://doi.org/10.1016/j.quaint.2015.10.034

Berger, G.W., Pérez-González, A., Carbonell, E., Arsuaga, J.L., Bermúdez de Castro, J.M., Ku, T.L., 2008. Luminescence chronology of cave sediments at the Atapuerca paleoanthropological site, Spain. Journal of Human Evolution 55, 300-311.

Bermejo, L., Ortega, A.I., Guérin, R., Benito-Calvo, A., Pérez-González, A., Parés, J. M., Aracil, E., Bermúdez de Castro, J. M., Carbonell, E., 2017. 2D and 3D ERT imaging for identifying karst morphologies in the archaeological sites of Gran Dolina and Galería Complex (Sierra de Atapuerca, Burgos, Spain). Quat. Int. 433, 393-401.

Bermejo, L., Ortega, A.I., Parés, J.M., Campaña, I., Bermúdez de Castro, J.M., Carbonell, E., Conyers, L.B., 2020. Karst features interpretation using ground-penetrating radar: a study from the Sierra de Atapuerca, Spain. Geomorphology 367, 1–14.

Bermúdez De Castro, J.M., Arsuaga, J.L., Carbonell, E., Rosas, A., Martínez, I., Mosquera, M., 1997. A hominid from the lower Pleistocene of Atapuerca, Spain: Possible ancestor to Neandertals and modern humans. Science 276, 1392–1395.

Bermúdez de Castro, J.M., Martinón-Torres, M., Arsuaga, J.L., Carbonell, E., 2017. Twentieth anniversary of Homo antecessor (1997-2017): A review. Evolutionary Anthropology: Issues, News, and Reviews, 26(4), 157-171. https://doi.org/10.1002/evan.21540

Bermúdez de Castro, J.M., Pérez-González, A., Martinón-Torres, M., Gómez-Robles, A., Rosell, J., Prado, L., Sarmiento, S., Carbonell, E., 2008. A new early Pleistocene hominin mandible from Atapuerca-TD6, Spain. J. Hum. Evol. 55, 729–735.

Berna, F., Matthews, A., and Weiner, S., 2004. Solubilities of bone mineral from archaeological sites: the recrystallization window. Journal of Archaeological Science, 31(7), 867–882.

Blain, H.-A., Bailon, S., Cuenca-Bescós, G., Arsuaga, J.L., Bermúdez de Castro, J.M., Carbonell, E., 2009. Long-term climate record inferred from early-middle Pleistocene amphibian and squamate reptile assemblages at the Gran Dolina Cave, Atapuerca, Spain. Journal of Human Evolution, 56(1), Article 1. https://doi.org/10.1016/j.jhevol.2008.08.020

Blanchard, S.C., Chasteen, N.D., 1976. Determination of manganese(II) in powdered barnacle shells by electron paramagnetic resonance. Analytica Chimica Acta 82(1), 113-119.

Blasco, R., Rosell, J., Domínguez-Rodrigo, M., Lozano, S., Pastó, I., Riba, D., Vaquero, M., Peris, J.F., Arsuaga, J.L., de Castro, J.M.B., Carbonell, E., 2013. Learning by Heart: Cultural Patterns in the Faunal Processing Sequence during the Middle Pleistocene. PLoS ONE 8.

Campaña, I., 2018. Estratigrafía y sedimentología del yacimiento de Gran Dolina (Sierra de Atapuerca, Burgos). Universidad de Burgos. https://doi.org/10.36443/10259/5550.

Campaña, I., Benito-Calvo, A., Pérez-González, A., Ortega, A.I., Bermúdez de Castro, J.M., Carbonell, E., 2017. Pleistocene sedimentary facies of the Gran Dolina archaeo-paleoanthropological site (Sierra de Atapuerca, Burgos, Spain). Quat. Int. 433, 68-84. https:// doi. org/ 10. 1016/j. quaint. 2015. 04. 023

Campaña, I., Benito-Calvo, A., Pérez-González, A., Álvaro-Gallo, A., Miguens-Rodríguez, L., Iglesias-Cibanal, J., Bermúdez de Castro, J.M., Carbonell, E., 2022. Revision of TD1 and TD2 stratigraphic sequence of Gran Dolina cave (Sierra de Atapuerca, Spain). J. Iber. Geol. 48, 425–443. https://doi.org/10.1007/s41513-022-00200-8.

Campaña, I., Benito-Calvo, A., Pérez-González, A., Ortega, A.I., Álvaro-Gallo, A., Miguens-Rodríguez, L., Iglesias-Cibanal, J., Bermúdez de Castro, J.M., Carbonell, E., 2023. Reconstructing depositional environments through cave interior facies: The case of Galería Complex (Sierra de Atapuerca, Spain). Geomorphology 108864. https://doi.org/10.1016/j.geomorph.2023.108864.

Campaña, I., Pérez-González, A., Benito-Calvo, A., Rosell, J., Blasco, R., De Castro, J.M.B., Carbonell, E., Arsuaga, J.L., 2016. New interpretation of the Gran Dolina-TD6 bearing Homo antecessor deposits through sedimentological analysis. Scientific Reports, 6. Scopus. https://doi.org/10.1038/srep34799

Carbonell, E., Bermúdez De Castro, J.M., Arsuaga, J.L., Diez, J.C., Rosas, A., Cuenca-Bescós, G., Sala, R., Mosquera, M., Rodríguez, X.P., 1995. Lower pleistocene hominids and artifacts from Atapuerca-TD6 (Spain). Science 269, 826–830.

Carbonell, E., Bermúdez De Castro, J.M., Parés, J.M., Pérez-González, A., Cuenca-Bescós, G., Ollé, A., Mosquera, M., Huguet, R., Van Der Made, J., Rosas, A., Sala, R., Vallverdú, J., García, N., Granger, D.E., Martinón-Torres, M., Rodríguez, X.P., Stock, G.M., Vergès, J.M., Allué, E., Burjachs, F., Cáceres, I., Canals, A., Benito, A., Díez, C., Lozano, M., Mateos, A., Navazo, M., Rodríguez, J., Rosell, J., Arsuaga, J.L., 2008. The first hominin of Europe. Nature 452, 465–469.

Cheng, H., Edwards, R.L., Shen, C.C., Polyak, V.J., Asmerom, Y., Woodhead, J., Hellstrom, J., Wang, Y., Kong, X., Spötl C., Wang, X., Alexander Jr., E.C., 2013. Improvements in 230Th dating, 230Th and 234U half-life values, and U-Th isotopic measurements by multi-collector inductively coupled plasma mass spectroscopy. Earth Planet. Sc. Lett. 371–372, 82–91.

Cuenca-Bescós, G., García, N., 2007. Biostratigraphic succession of the Early and Middle Pleistocene mammal faunas of the Atapuerca cave sites (Burgos, Spain). Cour. Forsch.- Inst. Senckenberg 259, 99-110.

Cuenca-Bescós, G., Blain, H.-A., Rofes, J., Lozano-Fernández, I., López-García, J.M., Duval, M., Galán, J., Núñez-Lahuerta, C., 2015. Comparing two different Early Pleistocene microfaunal sequences from the caves of Atapuerca, Sima del Elefante and Gran Dolina (Spain): Biochronological implications and significance of the Jaramillo subchron. Quat. Int. 389, 148-158.

Cuenca-Bescós, G., Blain, H.-A., Rofes, J., López-García, J.M., Lozano-Fernández, I., Galán, J., Núñez-Lahuerta, C., 2016. Updated Atapuerca biostratigraphy: small mammal distribution and its implications for the biochronology of the Quaternary in Spain. Comptes Rendus Palevol 15, 621–634. https://doi.org/10.1016/j.crpv.2015.09.006.

Demuro, M., Arnold, L.J., Parés, J.M., Pérez-González, A., Ortega, A.I., Arsuaga, J.L., Bermúdez de Castro, J.M., Carbonell, E., 2014. New luminescence ages for the Galería Complex

archaeological site: resolving chronological uncertainties on the Acheulean record of the Sierra de Atapuerca, Northern Spain. PLoS ONE 9 (10).

Demuro, M., Arnold, L.J., Parés, J.M., Aranburu, A., Huguet, R., Vallverdú, J., Arsuaga, J.L., Bermúdez de Castro, J.M., Carbonell, E., 2022. Extended-range luminescence chronologies for the Middle Pleistocene units at the Sima del Elefante archaeological site (Sierra de Atapuerca, Burgos, Spain). Quat. Geochr. 71, 101318.

Douville, E., Salle, E., Frank, N., Eisele, M., Pons-Branchu, E., Ayrault, S., 2010. Rapid and accurate U-Th dating of ancient carbonates using inductively coupled plasma-quadrupole mass spectrometry. Chem. Geol. 272, 1–11.

Duval, M., 2015. Electron Spin Resonance Dating of fossil tooth enamel, in Rink, W.J., Thompson, J.W. (Eds.) Encyclopedia of Scientific Dating Methods, Springer Netherlands, pp. 239-246. DOI: 10.1007/978-94-007-6304-3_71. ISBN 978-94-007-6304-3.

Duval, M., Grün, R., 2016. Are published ESR dose assessments on fossil tooth enamel reliable? Quat. Geochronol. 31, 19–27.

Duval, M., Falguères, C., Bahain, J.-J., 2012. Age of the oldest hominin settlements in Spain: Contribution of the combined U-series/ESR dating method applied to fossil teeth. Quat. Geochronol. 10, 412-417.

Duval, M., Guilarte Moreno, V., Grün, R., 2013. ESR dosimetry of fossil enamel: some comments about measurement precision, long-term signal fading and dose–response curve fitting. Radiat. Protect. Dosim. 157 (4), 463–476.

Duval, M., Falguères, C., Bahain, J.-J., Grün, R., Shao, Q., Aubert, M., Hellstrom, J., Dolo, J.-M., Agusti, J., Martínez-Navarro, B., Palmqvist, P. and Toro-Moyano, I., 2011. The challenge of dating early pleistocene fossil teeth by the combined uranium series–electron spin resonance method: the Venta Micena palaeontological site (Orce, Spain). J. Quaternary Sci., 26: 603-615. https://doi.org/10.1002/jqs.1476

Duval, M., Grün, R., Parés, J. M., Martín-Francés, L., Campaña, I., Rosell, J., Shao, Q., Arsuaga, J. L., Carbonell, E., Bermúdez de Castro, J. M., 2018. The first direct ESR dating of a hominin tooth from Atapuerca Gran Dolina TD-6 (Spain) supports the antiquity of Homo antecessor. Quaternary Geochronology, 47, 120–137.

Duval, M., Voinchet, P., Arnold, L.J., Parés, J.M., Minnella, W., Guilarte, V., Demuro, M., Falguères, C., Bahain, J.-J., Despriée, J., 2020. A multi-technique dating study of two lower palaeolithic sites from the cher valley (Middle Loire catchment, France): Lunery-la Terre-des-Sablons and Brinay-la Noira. Quat. Int. 556, 71–87. https://doi.org/10.1016/j.quaint.2020.05.033.

Duval, M., Arnold, L.J., Demuro, M., Parés, J.M., Campaña, I., Carbonell, E., Bermúdez de Castro, J.M., 2022. New chronological constraints for the lowermost stratigraphic unit of Atapuerca Gran Dolina (Burgos, N Spain). Quat. Geochronol. 71, 101292 https://doi.org/10.1016/j.quageo.2022.101292.

Eggins S.M., Grün R., McCulloch M.T., Pike A.W.G., Chappell J., Kinsley L., Mortimer G., Shelley M., Murray-Wallace C.V., Spötl C., Taylor L., 2005. In situ U-series dating by laser-ablation multi-collector ICPMS: New prospects for Quaternary geochronology. Qua. Sci. Rev. 24(23-24), 2523-2538.

Eggins, S., Grün, R., Pike, A.W.G., Shelley, M., Taylor, L., 2003. ^{238}U, ^{232}Th profiling and U-series isotope analysis of fossil teeth by laser ablation-ICPMS. Qua. Sci. Rev. 22(10-13), 1373-1382.

Elliott, J., 2002. Calcium phosphate biominerals. In: Kohn, M.J., Rakovan, J., Hughes, J.M. (Eds.), Phosphates – Geochemical, Geobiological and Material Importance. Mineralogical Society of America, Washington, DC, pp. 427–454.

Falguères, C., Bahain, J.-J., Bischoff, J.L., Pérez-González, A., Ortega, A.I., Ollé, A., Quiles, A., Ghaleb, B., Moreno, D., Dolo, J.-M., Shao, Q., Vallverdú, J., Carbonell, E., Bermúdez de Castro, J.M., Arsuaga, J.L., 2013. Combined esr/u-series chronology of acheulian hominid-bearing layers at trinchera galería site, atapuerca, spain. J. Hum. Evol. 65, 168–184.

Falguères, C., Bahain, J.J., Yokoyama, Y., Arsuaga, J.L., Bermudez De Castro, J.M., Carbonell, E., Bischoff, J.L., Dolo, J. M., 1999. Earliest humans in Europe: The age of TD6 Gran Dolina, Atapuerca Spain. Journal of Human Evolution, 37(3–4), 343–352.

Falguères, C., Bahain, J.J., Bischoff, J.L., Pérez-González, A., Ortega, A.I., Ollé, A., Quiles, A., Ghaleb, A., Moreno, D., Dolo, J.M., Shao, Q., Vallverdú, J., Carbonell, E., Bermúdez de Castro, J.M., Arsuaga, J.L., 2013. Combined ESR/U-series chronology of acheulian hominid-bearing layers at Trinchera Galería site, Atapuerca, Spain. J. Hum. Evol. 65(2), 168-184.

Fernández-Jalvo, Y., 1995. Small mammal taphonomy at la Trinchera de Atapuerca (Burgos Spain) A remarkable example of taphonomic criteria used for stratigraphic correlations and palaeoenvironment interpretations. Palaeo3 114, 167-195.

Friesem, D. E., Shahack-Gross, R., Weinstein-Evron, M., Teutsch, N., Weissbrod, L., Shimelmitz, R., 2021. High-resolution study of Middle Palaeolithic deposits and formation processes at Tabun Cave, Israel: Guano-rich cave deposits and detailed stratigraphic appreciation of Layer C. Quaternary Science Reviews 274, 107203.

Garba, R., Usyk, V., Ylä-Mella, L., Kameník, J., Stübner, K., Lachner, J., Rugel, G., Veselovský, F., Gerasimenko, N., Herries, A. I. R., Kučera, J., Knudsen, M. F., Jansen, J. D., 2024. East-to-west human dispersal into Europe 1.4 million years ago. Nature, 627(8005), 805-810. Scopus. https://doi.org/10.1038/s41586-024-07151-3

Gradstein, F., Ogg, J.G., Schmitz, M.D., Ogg, G.M., 2020. Geologic Time Scale 2020. ISBN: 9780128243619.

Grün, R., 2000. An alternative model for open system U-series/ESR age calculations: (closed system U-series)-ESR, CSUS-ESR. Ancient TL 18 (1), 1–4.

Grün, R., 2009. The DATA program for the calculation of ESR age estimates on tooth enamel. Quat. Geochronol. 4 (3), 231–232.

Grün, R., Eggins, S., Kinsley, L., Moseley, H., Sambridge, M., 2014. Laser ablation U-series analysis of fossil bones and teeth. Palaeogeography, Palaeoclimatology, Palaeoecology 416, 150-167.

Grün, R., Rhodes, E.J., 1991. On the selection of dose points for saturating exponential ESR/TL dose response curves. Ancient TL 9(3), 40-46.

Grün, R., Schwarcz, H.P., Chadam, J., 1988. ESR dating of tooth enamel: Coupled correction for U-uptake and U-series disequilibrium. International Journal of Radiation Applications and Instrumentation. Part D. Nuclear Tracks and Radiation Measurements 14(1-2), 237-241.

Grün, R., Katzenberger-Apel, O., 1994. An alpha irradiator for ESR dating. Ancient TL 12(2), 35–38.

Hayes, R.B., Haskell, E.H., Kenner, G.H., 1998. An assessment of the Levenberg-Marquardt fitting algorithm on saturating exponential data sets. Ancient TL 16(2), 57-62.

Hedges, R. E. M., Millard, A. R., 1995. Bones and groundwater: towards the modelling of diagenetic processes. Journal of Archaeological Science, 22(2), 155–164.

Hellstrom, J., 2006. U-Th dating of speleothems with high initial 230Th using stratigraphical constraint. Quaternary Geochronology 1, 289-295.

Hernando-Alonso, I., Moreno, D., Ortega, A. I., Benito-Calvo, A., Alonso, M. J., Campaña, I., Parés, J. M., Cáceres, I., García-Medrano, P., Carbonell, E., Bermúdez de Castro, J. M., 2024. ESR chronology of the endokarstic deposits of Galería complex (Sierra de Atapuerca, Spain). Quaternary Geochronology, 83, 101575. https://doi.org/10.1016/j.quageo.2024.101575

Hill, C.A., Forti, P., 1997. Cave Minerals of the world, Segunda edición. ed. National Speleological Society.

Hiess J, Condon D.J., McLean N., Noble S.R., 2012. 238U/235U Systematics in terrestrial uranium-bearing minerals. Science 335(6076), 1610-4.

Huguet, R., Vallverdú, J., Rodríguez-Álvarez, X. P., Terradillos-Bernal, M., Bargalló, A., Lombera-Hermida, A., Menéndez, L., Modesto-Mata, M., Van der Made, J., Soto, M., Blain, H.-A., García, N., Cuenca-Bescós, G., Gómez-Merino, G., Pérez-Martínez, R., Expósito, I., Allué, E., Rofes, J., Burjachs, F., Canals, A., Bennàsar, M., Nuñez-Lahuerta, C., Bermúdez de Castro, J.M., Carbonell, E., 2017. Level TE9c of Sima del Elefante (Sierra de Atapuerca, Spain): A comprehensive approach. What's happening now in Atapuerca? Latest research at the Sierra de Atapuerca sites, 433, 278-295. https://doi.org/10.1016/j.quaint.2015.11.030Karkanas, P.,2017. Chemical Alteration. In: Gilbert A.S. (eds) Encyclopedia of Geoarchaeology. Encyclopedia of Earth Sciences Series. Springer, Dordrecht. https://doi.org/10.1007/978-1-4020-4409-0_126

Karkanas, P., Bar-Yosef, O., Goldberg, P., Weiner, S., 2000. Diagenesis in Prehistoric Caves: the Use of Minerals that Form In Situ to Assess the Completeness of the Archaeological Record. J. Archaeol. Sci. 27, 915–929.

Karkanas, P., Kyparissi-Apostolika, N., Bar-Yosef, O., Weiner, S., 1999. Mineral assemblages in Theopetra, Greece: A framework for understanding diagenesis in a prehistoric cave. J. Archaeol. Sci. 26, 1171–1180.

Karkanas, P., Rigaud, J.P., Simek, J.F., Albert, R.M., Weiner, S., 2002. Ash Bones and guano: a study of the minerals and phytoliths in the sediments of Grotte XVI, Dordogne, France. J. Archaeol. Sci. 29 (7), 721–732.

Krauskopf, K. B., 1979. Introduction to Geochemistry, 2nd edition. New York: McGraw-Hill Co.

Marsh, R.E., 1999. Beta-gradient Isochrons Using Electron Paramagnetic Resonance: towards a New Dating Method in Archaeology. MSc thesis. McMaster University, Hamilton.

Martinez, M., Woda, C., Walther, R., Mangini, A., 2001. An analytical model for the SO2− centre, ESR signal at g=2.0057 in carbonates. Applied Radiation and Isotopes, 54(6), 995-1003. https://doi.org/10.1016/S0969-8043(00)00374-2

Moreno, D., 2011. Datation par ESR de quartz optiquement blanchis (ESR-OB) de la région de Atapuerca (Burgos, Espagne). Application au site préhistorique de Gran Dolina (contexte karstique) et aux systèmes fluviatiles quaternaires de l'Arlanzón et l'Arlanza. Universitat Rovira i Virgili, Tarragona (Spain). Muséum National D'Histoire Naturelle, Paris (France).

Moreno, D., Falguères, C., Pérez-González, A., Voinchet, P., Ghaleb, B., Despriée, J., Bahain, J.-J., Sala, R., Carbonell, E., Bermúdez de Castro, J.M., Arsuaga, J.L., 2015. New radiometric dates on the lowest stratigraphical section (TD1 to TD6) of Gran Dolina site (Atapuerca, Spain). Quaternary Geochronology, 30, 535–540.

Ollé, A., Mosquera, M., Rodríguez, X.P., de Lombera-Hermida, A., García-Antón, M.D., García-Medrano, P., Peña, L., Menéndez, L., Navazo, M., Terradillos, M., Bargalló, A., Márquez, B., Sala, R., Carbonell, E., 2013. The Early and Middle Pleistocene technological record from Sierra de Atapuerca (Burgos, Spain). Quat. Int. 295, 138–167.

Onac, B. P., 2011. Minerals. In: Culver, D. C., White, W. B. (Eds.), Encyclopedia of caves (2nd ed.).

Onac B. P., Forti, P., 2011. Minerogenetic mechanisms occuring in the cave environment: an overview. Int. J. of Speleo. 40(2), 79-98.

Ortega, A.I., 2009. La Evolución Geomorfológica del karst de la Sierra de Atapuerca (Burgos) y su relación con los yacimientos pleistocenos que contiene. Universidad de Burgos, Facultad de Humanidades y Educación. Departamento de ciencias históricas y geografía, Burgos.

Ortega, A.I., Benito-Calvo, A., Pérez-González, A., Martín Merino, M.A., Pérez-Martínez, R., Parés, J.M., Aramburu, A., Arsuaga, J.L., Bermúdez de Castro, J.M., Carbonell, E., 2013. Evolution of multilevel caves in the Sierra de Atapuerca (Burgos, Spain) and its relation to human occupation. Geomorphology 122–133. https://doi.org/10.1016/j.geomorph.2012.05.031

Ortega, A.I., Benito-Calvo, A., Pérez-González, A., Carbonell, E., Bermúdez de Castro, J.M., Arsuaga, J.L., 2014. Atapuerca Karst and its Palaeoanthropological Sites, in: Gutiérrez, F., Gutiérrez, M. (Eds.), Landscapes and Landforms of Spain, World Geomorphological Landscapes. Springer Netherlands, Dordrecht, pp. 101–110. https://doi.org/10.1007/978-94-017-8628-7_8

Parés, J.M., Álvarez, C., Sier, M., Moreno, D., Duval, M., Woodhead, J.D., Ortega, A.I., Campaña, I., Rosell, J., Bermúdez de Castro, J.M., Carbonell, E., 2018. Chronology of the cave interior sediments at Gran Dolina archeological site, Atapuerca (Spain). Quat. Sci. Rev. 186, 1–16.

Parés, J.M., Arnold, L., Duval, M., Demuro, M., Pérez-González, A., Bermúdez de Castro, J.M., Carbonell, E., Arsuaga, J.L., 2013. Reassessing the age of Atapuerca-TD6 (Spain): New paleomagnetic results. J. Archaeol. Sci. 40, 4586–4595.

Parés, J.M., Pérez-González, A., 1999. Magnetochronology and stratigraphy at Gran Dolina section, Atapuerca (Burgos, Spain). J. Hum. Evol. 37, 325–342.

Parés, J.M., Pérez-González, A., Rosas, A., Benito, A., Bermúdez de Castro, J.M., Carbonell, E., Huguet, R., 2006. Matuyama-age lithic tools from the Sima del Elefante site, Atapuerca (northern Spain). J. Hum. Evol. 50, 163–169.

Pérez-González, A., Aleixandre, T., Pinilla, A., Gallardo, J., Benayas, J., Martínez, M.J., 1995. Aproximación a la estratigrafía de galería en la trinchera de la Sierra de Atapuerca (Burgos). In: Bermúdez de Castro, J.M., Arsuaga, J.L., Carbonell, E. (Eds.), Evolución Humana En Europa y Los Yacimientos de La Sierra de Atapuerca. Junta de Castilla y León, Consejería de Cultura y Turismo, Valladolid, pp. 99–122.

Pérez-González, A., Parés, J.M., Carbonell, E., Aleixandre, T., Ortega, A.I., Benito, A., Martin Merino, M.A., 2001. Géologie de la Sierra de Atapuerca et stratigraphie des remplissages karstiques de Galería et Dolina (Burgos, Espagne). L'Anthropologie 105, 27–43.

Pérez-González, A., Parés, J.M., Gallardo, J., Aleixandre, T., Ortega, A.I., Pinilla, A., 1999. Geología y estratigrafía del relleno de galería de la Sierra de Atapuerca (Burgos), in: Carbonell, E., Rosas, A., Díez, C. (Eds.), ATAPUERCA: Ocupaciones Humanas y Paleoecología Del Yacimiento de Galería. Junta de Castilla y León, Conserjeria de Educación y Cultura, Valladolid, pp. 31–42.

Pineda, A., Saladié, P., Expósito, I., Rodríguez-Hidalgo, A., Cáceres, I., Huguet, R., Rosas, A., López-Polín, L., Estalrrich, A., García-Tabernero, A., Vallverdú, J., 2017. Characterizing hyena coprolites from two latrines of the Iberian Peninsula during the Early Pleistocene: Gran Dolina (Sierra de Atapuerca, Burgos) and la Mina (Barranc de la Boella, Tarragona). Palaeogeography, Palaeoclimatology, Palaeoecology, 480, 1-17. https://doi.org/10.1016/j.palaeo.2017.04.021

Polisca, F., Dal Corso, M., Baldan, M., Bortolini, M., Battistel, D., Dal Sasso, G., Gherardi, F., Canti, M., Piazzalunga, G., Nicosia, C. 2025. Phosphatic crusts as macroscopic and microscopic proxies for identifying archaeological animal penning areas. Journal of Archaeological Science, 177, 106207. https://doi.org/10.1016/j.jas.2025.106207

Prescott, J.R., Hutton, J.T., 1994. Cosmic ray contributions to dose rates for luminescence and ESR dating: large depths and long-term time variations. Radiat. Meas. 23 (2–3), 497–500.

Rietveld, H.M., 1969. A profile refinement method for nuclear and magnetic structures. J. Appl. Crystallogr. 2, 65–71. https://doi.org/10.1107/S0021889869006558

Rink, W.J., Bartoll, J., Goldberg, P., Ronen, A., 2003. ESR dating of archaeologically relevant authigenic terrestrial apatite veins from Tabun Cave, Israel. J. Arch. Sci. 30(9), 1127-1138.

Rodríguez, J., Burjachs, F., Cuenca-Bescós, G., García, N., Van der Made, J., Pérez González, A., Blain, H.A., Expósito, I., López-García, J.M., García Antón, M., Allué, E., Cáceres, I., Huguet, R., Mosquera, M., Ollé, A., Rosell, J., Parés, J.M., Rodríuez, X.P., Díez, C., Rofes, J., Sala, R., Saladié, P., Vallverdú, J., Bennasar, M.L., Blasco, R., Bermúdez de Castro, J.M., Carbonell, E., 2011. One million years of cultural evolution in a stable environment at

Atapuerca (Burgos, Spain). Quat. Sci. Rev. 30, 1396-1412. https://doi.org/10.1016/j.quascirev.2010.02.021.

Rodríguez-Gómez, G., Rodríguez, J., Martín-González, J.T., Goikoetxea, I., Mateos, A., 2013. Modeling trophic resource availability for the first human settlers of Europe: The case of Atapuerca TD6. J. Hum. Evol. 64, 645–657.

Rosas, A., Huguet, R., Pérez-González, A., Carbonell, E., Bermúdez de Castro, J.M., Vallverdú, J., Van Der Made, J., Allué, E., García, N., Martínez-Pérez, R., Rodríguez, J., Sala, R., Saladie, P., Benito, A., Martínez-Maza, C., Bastir, M., Sánchez, A., Parés, J.M., 2006. The "Sima del Elefante" cave site at Atapuerca (Spain). Estud. Geol. 62, 327–348.

Rosas, A., Pérez-González, A., Carbonell, E., Van Der Made, J., Sánchez, A., Laplana, C., Cuenca-Bescós, G., Parés, J.M., Huguet, R., 2001. Le gisement pléistocène de la «Sima del Elefante» (Sierra de Atapuerca, Espagne). L'Anthropologie 105, 301–312.

Schiegl, S., Goldberg, P., Bar-Yosef, O., Weiner, S., 1996. Ash deposits in Hayonim and Kebara caves, Israel: macroscopic, microscopic and mineralogical observations, and their archaeological implications, Journal of Archaeological Science 23 763-781.

Shao, Q., Li, C., Huang, M., Liao, Z., Arps, J., Huang, C., Chou, Y., Kong, X., 2019. Interactive programs of MC-ICPMS data processing for 230Th/U geochronology. Quat. Geochronol. 51, 43–52.

Saladié, P., Huguet, R., Díez, C., Rodríguez-Hidalgo, A., Cáceres, I., Vallverdú, J., Rosell, J., Bermúdez De Castro, J.M., Carbonell, E., 2011. Carcass transport decisions in Homo antecessor subsistence strategies. J. Hum. Evol. 61, 425–446.

Saladié, P., Rodríguez-Hidalgo, A., Domínguez-Rodrigo, M., Vallverdú, J., Mosquera, M., Ollé, A., Huguet, R., Cáceres, I., Arsuaga, J.L., Bermúdez de Castro, J.M., Carbonell, E., 2021. Dragged, lagged, or undisturbed: Reassessing the autochthony of the hominin-bearing assemblages at Gran Dolina (Atapuerca, Spain). Archaeological and Anthropological Sciences, 13(4), 65. https://doi.org/10.1007/s12520-021-01303-6

Singer, B.S., Jicha, B.R., Mochizuki, N., Coe, R.S., 2019. Synchronizing volcanic, sedimentary, and ice core records of Earth's last magnetic polarity reversal. Sci. Adv. 5, eaaw4621.

Shahack-Gross, R., Berna, F., Karkanas, P., Weiner, S., 2004. Bat guano and preservation of archaeological remains in cave sites. J. Archaeol. Sci. 31, 1259–1272.

Stiner, M.C., Kuhn, S., Surovell, T. A., Goldberg, P., Meignen, L., Weiner, S., Bar-Yosef, O., 2001. Bone preservation in Hayonim Cave (Israel): a macroscopic and mineralogical study, Journal of Archaeological Science 28 643-659.

Vallverdú, J., 2002. Micromorfología de Las Facies Sedimentarias de La Sierra de Atapuerca y del Nivel J del Abric Romaní. Implicaciones Geoarqueológicas Y Paleoetnográficas. Universitat Rovira i Virgili, Tarragona (Spain).

Weiner, S., P. Goldberg, O. Bar-Yosef, Bone preservation in Kebara Cave, Israel using on-site Fourier Transform Infrared spectrometry, Journal of Archaeological Science 20 (1993) 613-

White, L.K., Szabo, A., Carkner, P., Chasteen, N.D., 1977. An electron paramagnetic resonance study of manganese(II) in the aragonite lattice of a clam shell, Mya arenaria. The Journal of Physical Chemistry, 81(14), 1420-1424. https://doi.org/10.1021/j100529a015

Yokoyama, Y., Bibron, R., Leger, C., 1988. ESR dating of palaeolithic calcite: A comparison between powder and monocrystal spectra with thermal annealing. Quaternary Science Reviews, 7(3), 433-438. https://doi.org/10.1016/0277-3791(88)90042-X

Table captions

Table 1: Basic description of the apatite samples collected for the present study.

Table 2: Quantitative mineralogy of the phosphate samples by X-ray diffraction (XRD), expressed in %.

Table 3: Chemical composition of phosphate samples using X-ray fluorescence (XRF), expressed in % weight. Key: < DL = below Detection Limit.

Table 4: U-series dating results obtained from solution analyses performed in 2017 (ESR13-05, ESR13-07 and ESR1310) and 2019 (other samples). ^{230}Th/U ages were calculated with the half-lives of 75,584 years and 245,620 years for ^{230}Th and ^{234}U, respectively (Cheng et al., 2013). U-series ages were corrected for the initial ^{230}Th contamination with assumed initial ^{230}Th/^{232}Th atonic ratio of (4.4 ± 2.2)×10^{-6}, which is a value for the material at secular equilibrium, with the bulk earth ^{232}Th/^{238}U value of 3.8 and an assumed error of 50%. The corrected ages are given on the "BP" scale, before 1950 A.D. (^{234}U/^{238}U)$_i$ represents the initial activity ratio of ^{234}U/^{238}U. All uncertainties are given at 2σ. Key: n.c. = not calculated (activity ratios above secular equilibrium).

Table 5: ESR data set. The average aliquot weight was derived from the weight of all aliquots of a given sample. Minimum S/N value corresponds to the average S/N value obtained from the various measurements of the natural aliquot of a given sample. Mean intensity precision corresponds to the variability (coefficient of variation) of the mean ESR intensities derived from all aliquots of a given sample on a given measurement time. D_E precision corresponds the relative standard deviation associated to the mean D_E value calculated form the three repeated measured. D_{max} is the maximum irradiation dose employed for the dose response curve fitting. D_{max}/D_E ratio follows the recommendations by Duval and Grün (2016).

Table 6: Radioelement concentrations measured in the apatite samples by ICP-OES/MS.

Table 7: Radioelement concentrations measured by ICP-OES/MS in diverse materials collected from the immediate surroundings of the ESR samples (see also Supplementary Material Fig. S1 and S2).

Table 8: Summary of data inputs used for the ESR age calculations. All errors are 1σ.

Table 9: ESR age results. Errors are 1σ. Calculations were performed using three different uranium uptake models: U-series (US; Grün et al., 1988), Early Uptake (EU), Closed-system US (CSUS; Grün, 2000).

Figure captions

Figure 1: A: Map of the Atapuerca multilevel cave system (modified from Ortega et al., 2013). The underground karstic infills of the map are indicated in pale green (Bermejo et al., 2020). B: aerial image of the Railway Trench with the situation of Gran Dolina, Galería Complex and Sima del Elefante. C: Cross-section of Gran Dolina, Galería Complex and Sima del Elefante sedimentary infill (modified from Campaña et al., 2023).

Figure 2: Composite stratigraphic sections of the three archaeo-paleontological sites studied in the present work (Gran Dolina: Campaña et al., 2017 and Campaña et al., 2022, Galería: Pérez-González et al., 1999, Falguères et al., 2013 and Campaña et al., 2023, and Sima del Elefante: Carbonell et al., 2008). The position of the ESR samples is indicated by a red star. The stratigraphic position of the main magnetic reversal observed at the three sites, which is tentatively attributed to the Brunhes-Matuyama transition is shown.

Figure 3: Pictures of the apatite samples in their original stratigraphic position, as indicated by the red arrows (left column, from A1 to H1), and once collected, in the laboratory before preparation (right column, from A2 to H2).

Figure 4: Cross-section of ESR13-08 showing Laser Ablation tracks 1 to 5 (red) and spots (back and white). Numerical results may be found in Supplementary Material Tables S1 to S5. Only finite U-series age results obtained from the authigenic apatite are displayed. The associated errors are not given to ease readability.

Figure 5: Wide ESR spectrum acquisitions (1000 G) carried out at room temperature for the natural samples ESR13-04 to ESR13-11. The ESR spectra of a calcite and limestone sample from Atapuerca are also displayed for comparison. Acquisition parameters are as follows: sweep width = 1000 G, resolution = 2048 points, modulation amplitude = 1 G, conversion time = 40 msec, time constant = 10 msec, microwave power = 1 mW, number of scans = 5. The red tringle arrow shows the radiation-induced signal typically measured in authigenic apatite, while the blue triangle arrow shows a signal of unknown origin that is visible in all samples. Finally, the six orange triangles show the stextet Mn lines present in the calcite and limestone samples.

Figure 6: Narrow ESR spectrum acquisitions (50 G) carried out at room temperature for the natural samples ESR13-04 to ESR13-11. The ESR spectra of a calcite and limestone sample from Atapuerca are also displayed for comparison. Acquisition parameters are as follows: sweep width = 50 G, resolution = 2048 points, modulation amplitude = 1 G, conversion time = 40 msec, time constant = 10 msec, microwave power = 1 mW, number of scans = 30. The green triangle arrow shows the signal possibly attributed to SO_2^- signal and resulting from the calcite (light green) for sample samples. The

narrow line observed in some samples (yellow triangle) is tentatively attributed to a transient signal induced by grinding. See text for further explanations. The position of the peaks T1, B1 and B2 associated to the radiation-induced ESR signal in authigenic apatite is indicated.

Figure 7: ESR dose response curves obtained for the eight samples. A zoomed plot of the dose range <1.1 kGy is also displayed. A SSE function (data weighting by $1/I^2$) was fitted through the experimental data points. Note that the fitting was not performed over the full dose range (i.e., Dmax = 9.4 kGy), but until a selected D_{max} in order to meet the D_{max}/D_E criterion defined by Duval and Grün (2016) (see main text for further explanations). The corresponding numerical fitting results may be found in Table 5.

Table 1.

Sample	Site	Stratigraphic unit	Basic description
ESR13-04	Galería	GII	- 4-mm thick laminated crust covering a limestone clast belonging to a sub-vertical debris fall
ESR13-05	Galería	GII	- 1-mm thick phosphate crust covering a limestone clast - Black and red coloring by manganese and iron oxides were observed in the surface of the crust
ESR13-06	Galería	GI	- Thin white powder-texture layer interpreted as a weathered speleothem
ESR13-07	Gran Dolina	TD4.1	- White phosphate crust covering a limestone clast.
ESR13-08	Gran Dolina	TD6.2	- < 2 cm-thick phosphate crust covering a highly weathered limestone clast - Lamination and manganese oxide were observed
ESR13-09	Gran Dolina	TD9	- White phosphate crust covering a limestone clast - Manganese oxide was observed inside the crust
ESR13-10	Gran Dolina	TD10.4	- 4-mm thick laminated phosphate crust from a limestone clast. - the lamination is formed by the alternation of about 0.5 mm thick pale brown and white lamina.
ESR13-11	Sima del Elefante	TE9	- Pale brown-yellowish powder-texture mud

Table 2.

Sample	Site	Stratigraphic unit	Calcite	Crandallite	Quartz	Phyllosilicate	Hydroxyapatite
ESR13-04	Galería	GII	0	0	0	0	100
ESR13-05	Galería	GII	15	0	0	0	85
ESR13-06	Galería	GI	0	55	7	9	30
ESR13-07	Gran Dolina	TD4	1	0	1	0	98
ESR13-08	Gran Dolina	TD6.2	23	0	0	0	77
ESR13-09	Gran Dolina	TD9	6	0	0	0	94
ESR13-10	Gran Dolina	TD10.4	3	0	0	0	97
ESR13-11	Sima del Elefante	TE9	7	0	11	10	72

Table 3.

Sample	Site	Unit	SiO_2	Al_2O_3	Fe_2O_3t	MnO	MgO	CaO	Na_2O	K_2O	TiO_2	P_2O_5	SO_3	LOI
ESR13-04	Galería	GII	0.44	0.32	0.10	<DL	0.04	53.21	0.24	0.04	<DL	37.69	<DL	7.91
ESR13-05	Galería	GII	0.20	0.19	0.06	0.06	0.05	53.86	0.25	0.03	<DL	31.64	<DL	13.67
ESR13-06	Galería	GI	12.71	21.53	2.77	0.03	0.32	21.98	0.30	0.65	0.22	24.27	<DL	15.32
ESR13-07	Gran Dolina	TD4	1.15	0.32	0.11	<DL	0.03	52.5	0.22	0.06	0.02	36.60	<DL	8.99
ESR13-08	Gran Dolina	TD6.2	0.42	0.39	0.13	0.07	0.07	53.45	0.31	0.05	0.02	29.28	<DL	15.79
ESR13-09	Gran Dolina	TD9	0.28	0.34	0.08	0.03	0.04	53.81	0.27	0.03	<DL	35.53	<DL	9.60
ESR13-10	Gran Dolina	TD10.4	0.45	0.45	0.12	0.05	0.04	52.96	0.27	0.04	<DL	36.13	0.05	9.43
ESR13-11	Sima del Elefante	TE9	16.3	4.22	1.52	0.05	0.32	40.96	0.21	0.72	0.26	25.52	0.07	9.88

Table 4.

Sample ID	Site	Sample weight (mg)	^{238}U (ppb)	^{232}Th (ppb)	$^{234}U/^{238}U$	$^{230}Th/^{234}U$	$^{230}Th/^{232}Th$	Age (ka)	Corrected age (ka BP)	$(^{234}U/^{238}U)_i$
ESR13-04	Galería	9.69	2431 ± 2	175.0 ± 0.2	1.2753 ± 0.0008	0.9565 ± 0.0013	51.780 ± 0.0873	253.1 ± 1.2	251.8 ± 1.4	1.560 ± 0.003
ESR13-05	Galería	59.7	28686 ± 163	103.4 ± 0.5	1.0590 ± 0.0077	0.3288 ± 0.0032	288.42 ± 1.6510	43.3 ± 0.5	43.1 ± 0.5	1.067 ± 0.009
ESR13-06	Galería	11.6	23128 ± 12	5091 ± 12	1.3711 ± 0.0009	1.3798 ± 0.0036	26.264 ± 0.0921	n.c.	n.c.	n.c.
ESR13-07	Gran Dolina	37.4	17791 ± 68	95.3 ± 0.4	1.0623 ± 0.0056	0.6490 ± 0.0047	384.40 ± 1.9613	112.5 ± 1.5	112.3 ± 1.5	1.086 ± 0.008
ESR13-08	Gran Dolina	7.31	11448 ± 2	218.3 ± 0.3	1.0431 ± 0.0005	0.6662 ± 0.0009	111.44 ± 0.2012	118.2 ± 0.3	117.7 ± 0.4	1.061 ± 0.0007
ESR13-09	Gran Dolina	11.1	28118± 4	115.6 ± 0.2	1.2375 ± 0.0002	0.8430 ± 0.0016	775.43 ± 2.1898	180.5 ± 0.8	180.5 ± 0.8	1.395 ± 0.001
ESR13-10	Gran Dolina	78.0	38760 ± 25	130.3 ± 0.5	1.2181 ± 0.0100	0.8211 ± 0.0091	888.75 ± 4.7432	171.0 ± 4.7	170.9 ± 4.7	1.353 ± 0.016
ESR13-11	Sima del Elefante	11.6	25316 ± 5	2770 ± 5	1.1364 ± 0.0003	1.0042 ± 0.0020	31.881 ± 0.0886	362.2 ± 5.0	359.9 ± 5.2	1.377 ± 0.006

Table 5.

Sample	Average aliquot weight (mg)	Minimum S/N	Measurement repeatability		D_E (Gy)	Adjusted r^2	D_{max} (Gy)	D_{max}/D_E
			Mean intensity precision	D_E precision (%)				
ESR1304	58.2	25.4	1.0	1.4	215 ± 7	0.9994	2148	10.0
ESR1305	58.2	24.2	0.4	3.1	267 ± 9	0.9993	2148	8.0
ESR1306	22.2	23.0	0.6	6.2	1630 ± 770	0.9270	3850	2.4
ESR1307	58.7	31.7	0.8	1.4	265 ± 11	0.9989	2148	8.1
ESR1308	38.4	25.6	0.1	1.3	596 ± 37	0.9971	3850	6.5
ESR1309	58.6	>100	1.0	0.4	1161 ± 102	0.9975	2148	1.8
ESR1310	55.5	78.3	0.2	0.5	882 ± 70	0.9959	3850	4.4
ESR1311	43.4	14.8	4.5	10.1	1247 ± 850	0.8751	2148	1.7

Table 6.

Sample ID	U (ppm)	Th (ppm)	K (%)
ESR13-04	0.52+0.07	0.30+0.05	0.0385+0.0021
ESR13-05	23.5+0.83	0.15+0.05	0.0118+0.0015
ESR13-06	12.5+0.44	8.98+0.38	0.8653+0.0340
ESR13-07	21.5+0.76	0.22+0.05	0.0431+0.0022
ESR13-08	17.7+0.62	0.40+0.05	0.0399+0.0021
ESR13-09	19.4+0.68	0.34+0.05	0.0423+0.0022
ESR13-10	34.6+1.22	0.23+0.05	0.0296+0.0019
ESR13-11	31.1+1.09	4.06+0.18	0.5456+0.0215

Table 7.

Corresponding ESR sample		Type	U (ppm)	Th (ppm)	K (%)
ESR13-04	A	Sediment	3.20±0.13	14.44±0.61	1.707±0.067
	B[1]	Limestone	0.22±0.07	0.09±0.05	0.011±0.002
	C	Limestone	0.33±0.07	0.14±0.05	0.005±0.001
	D	Limestone	0.24±0.07	0.17±0.05	0.024±0.002
	E	Limestone	0.21±0.07	0.11±0.05	0.005±0.001
ESR13-05	A	Sediment	4.08±0.16	17.03±0.71	1.629±0.064
	B	Limestone	0.21±0.07	0.07±0.05	0.008±0.001
	C	Limestone	0.18±0.07	0.11±0.05	0.004±0.001
	D[1]	Limestone	0.58±0.07	0.05±0.05	0.003±0.001
ESR13-06	A	Sediment	2.38±0.11	14.85±0.62	1.499±0.059
	C	Sediment	2.27±0.11	13.59±0.57	1.595±0.063
	D[2]	Sediment	2.94±0.12	25.33±1.06	1.875±0.074
ESR13-07	A	Sediment	1.53±0.09	5.84±0.25	0.768±0.030
	B	Sediment	3.18±0.13	7.16±0.30	0.911±0.036
	D[1]	Limestone	0.25±0.07	0.04±0.05	0.004±0.001
ESR13-08	A	Sediment	6.07±0.22	11.21±0.47	1.422±0.056
	B	Limestone	0.52±0.07	0.11±0.05	0.016±0.002
	C	Limestone	0.45±0.07	0.23±0.05	0.021±0.002
ESR13-09	A	Sediment	2.46±0.11	13.87±0.58	1.418±0.056
	C	Sediment	2.11±0.10	15.41±0.65	1.516±0.059
	E[2]	Sediment	2.54±0.11	7.69±0.33	0.969±0.038
ESR13-10	A	Sediment	6.20±0.23	15.00±0.63	1.509±0.059
	B[1]	Limestone	0.38±0.07	0.15±0.05	0.020±0.002
ESR13-11	B	Sediment	5.71±0.21	10.25±0.43	1.574±0.062
	C	Sediment	16.03±0.57	9.73±0.41	1.420±0.056

[1] Clast directly attached to the authigenic apatite sample being dated

[2] Sediment collected during sample preparation.

Table 8.

	Sample	ESR13-04	ESR13-05	ESR13-07	ESR13-08	ESR13-09	ESR13-10
	Layer	**GII**	**GII**	**TD4**	**TD6-2**	**TD9**	**TD10**
Authigenic apatite	D_E (Gy) (1)	215 ± 8.31	267 ± 10.6	265 ± 12.5	596 ± 39.1	1161 ± 105.3	882 ± 72.6
	U (ppm) (2)	1.475 ± 0.955	26.09 ± 2.593	17.67 ± 1.875	14.56 ± 3.116	23.77 ± 4.349	36.70 ± 2.060
	$^{234}U/^{238}U$ (3)	1.275 ± 0.001	1.059 ± 0.004	1.062 ± 0.006	1.043 ± 0.001	1.238 ± 0.001	1.218 ± 0.005
	$^{230}Th/^{234}U$ (3)	0.957 ± 0.001	0.329 ± 0.002	0.649 ± 0.002	0.666 ± 0.001	0.843 ± 0.001	0.821 ± 0.005
	Water	0	0	0	0	0	0
	Alpha efficiency	0.13 ± 0.02	0.13±0.02	0.13 ± 0.02	0.13 ± 0.02	0.13 ± 0.02	0.13 ± 0.02
	Total thickness (µm)	5757 ± 576	4109 ± 411	3720 ± 372	3716 ± 372	6189 ± 619	3250 ± 325
	Removed thickness side 1 (limestone block) (µm)	780 ± 78	681 ± 68	357 ± 36	84 ± 8	1551 ± 155	136 ± 14
	Removed thickness side 2 (sediment) (µm)	620 ± 62	956 ± 96	258 ± 26	602 ± 60	1611 ± 161	464 ± 46
	Density	2.95	2.95	2.95	2.95	2.95	2.95
Limestone block	U (ppm)	0.220 ± 0.069	0.580 ± 0.072	0.250 ± 0.069	0.485 ± 0.071	0.380 ± 0.070	0.380 ± 0.070
	Water	0	0	0	0	0	0
Sediment	U (ppm)	3.20 ± 0.13	4.08 ± 0.16	2.36 ± 0.11	6.07 ± 0.22	2.54 ± 0.11	6.20 ± 0.23
	Th (ppm)	14.44 ± 0.61	17.03 ± 0.71	6.50 ± 0.28	11.2 ± 0.47	7.69 ± 0.33	15.0 ± 0.63
	K (%)	1.71 ± 0.07	1.63±0.06	0.84 ± 0.03	1.42 ± 0.06	0.97 ± 0.04	1.51 ± 0.06
	Water content (% wet weight)	20 ± 5	20 ± 5	20 ± 5	20 ± 5	20 ± 5	20 ± 5
	Gamma dose rate (µGy/a)	368 ± 26 (4)	960 ± 40 (5)	543 ± 27 (4)	912 ± 46 (4)	757 ± 31 (5)	936 ± 39 (5)
	Depth (m)	10 ± 2	9 ± 2	14 ± 2	10 ± 2	7 ± 2	7 ± 2

(1) A 2.3% error on the dose rate delivered by the gamma source was added to the fitting error given in Table 5.

(2) For each sample, average uranium concertation values and associated standard error were considered (derived from Tables 4 and 6) in the ESR age calculation (see text for explanation).

(3) U-series data from Table 4 (values have been rounded to 3 decimal places, and errors are given at 1 σ).

(4) Derived from laboratory analysis (Supplementary Material Table S1).

(5) Derived from in situ measurement (Supplementary Material Table S1).

Table 9.

Sample	ESR13-04	ESR13-05	ESR13-07	ESR13-08	ESR13-09	ESR13-10
Layer	**GII**	**GII**	**TD4**	**TD6.2**	**TD9**	**TD10**
US-ESR age calculation						
US-ESR age (ka)	no result	no result	no result	no result	no result	no result
EU-ESR age calculation						
Internal dose rate (µGy/a)	652 ± 336	5279 ± 586	4300 ± 459	4137 ± 741	8373 ± 1295	10335 ± 920
Beta dose rate limestone (µGy/a)	0 ± 0	0 ± 0	0 ± 0	1 ± 1	0 ± 0	1 ± 0
Beta dose rate sediment (µGy/a)	7 ± 2	6 ± 2	18 ± 3	15 ± 3	0 ± 0	27 ± 6
Gamma + cosmic dose rate (µGy/a)	428 ± 28	1026 ± 41	586 ± 27	974 ± 92	843 ± 35	1022 ± 42
Total dose rate (µGy/a)	1087 ± 337	6311 ± 587	4904 ± 460	5127 ± 746	9216 ± 1296	11385 ± 921
EU-ESR Age (ka)	197 ± 61	42 ± 4	54 ± 5	116 ± 18	125 ± 21	77 ± 8
CSUS-ESR age calculation						
Modelled internal dose (Gy)	177 ± 1	226 ± 2	619 ± 5	483 ± 2	1703 ± 7	2350 ± 47

Figure 1

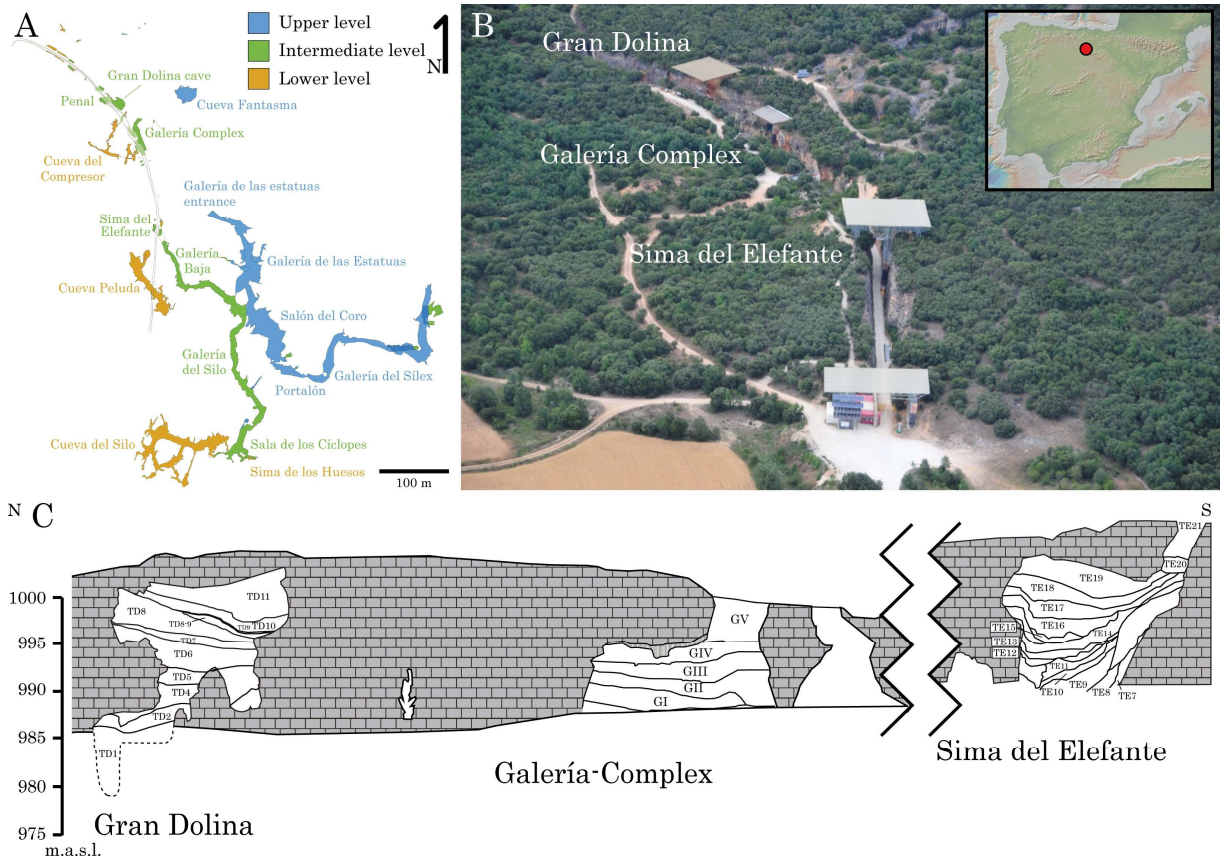
A
Upper level
Intermediate level
Lower level
N
Gran Dolina cave
Penal
Cueva Fantasma
Galería Complex
Cueva del Compresor
Galería de las estatuas entrance
Sima del Elefante
Galería Baja
Galería de las Estatuas
Cueva Peluda
Salón del Coro
Galería del Silo
Galería del Sílex
Portalón
Cueva del Silo
Sala de los Cíclopes
Sima de los Huesos
100 m
B
Gran Dolina
Galería Complex
Sima del Elefante
N C
S
1000
995
990
985
980
975
m.a.s.l.
TD1
TD2
TD4
TD5
TD6
TD8
TD8-9
TD10
TD11
GV
GIV
GIII
GII
GI
TE7
TE8
TE9
TE10
TE11
TE12
TE13
TE14
TE15
TE16
TE17
TE18
TE19
TE20
TE21
Gran Dolina
Galería-Complex
Sima del Elefante

Figure 2

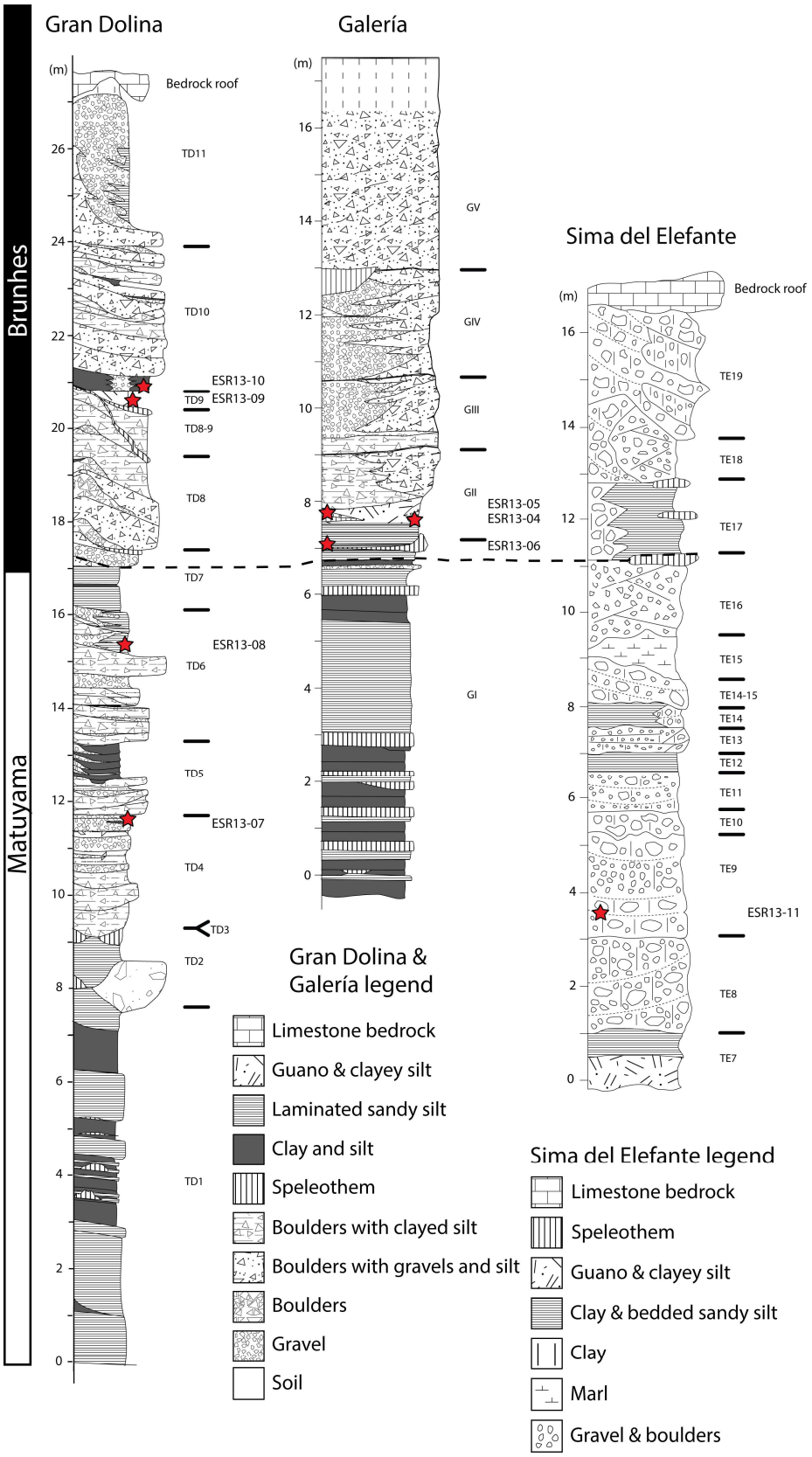
Brunhes
Matuyama
Gran Dolina
Galería
Sima del Elefante
(m)
Bedrock roof
TD11
TD10
ESR13-10
TD9
ESR13-09
TD8-9
TD8
TD7
ESR13-08
TD6
TD5
ESR13-07
TD4
TD3
TD2
TD1
GV
GIV
GIII
GII
ESR13-05
ESR13-04
ESR13-06
GI
TE19
TE18
TE17
TE16
TE15
TE14-15
TE14
TE13
TE12
TE11
TE10
TE9
ESR13-11
TE8
TE7
Gran Dolina & Galería legend
Limestone bedrock
Guano & clayey silt
Laminated sandy silt
Clay and silt
Speleothem
Boulders with clayed silt
Boulders with gravels and silt
Boulders
Gravel
Soil
Sima del Elefante legend
Limestone bedrock
Speleothem
Guano & clayey silt
Clay & bedded sandy silt
Clay
Marl
Gravel & boulders

Figure 3

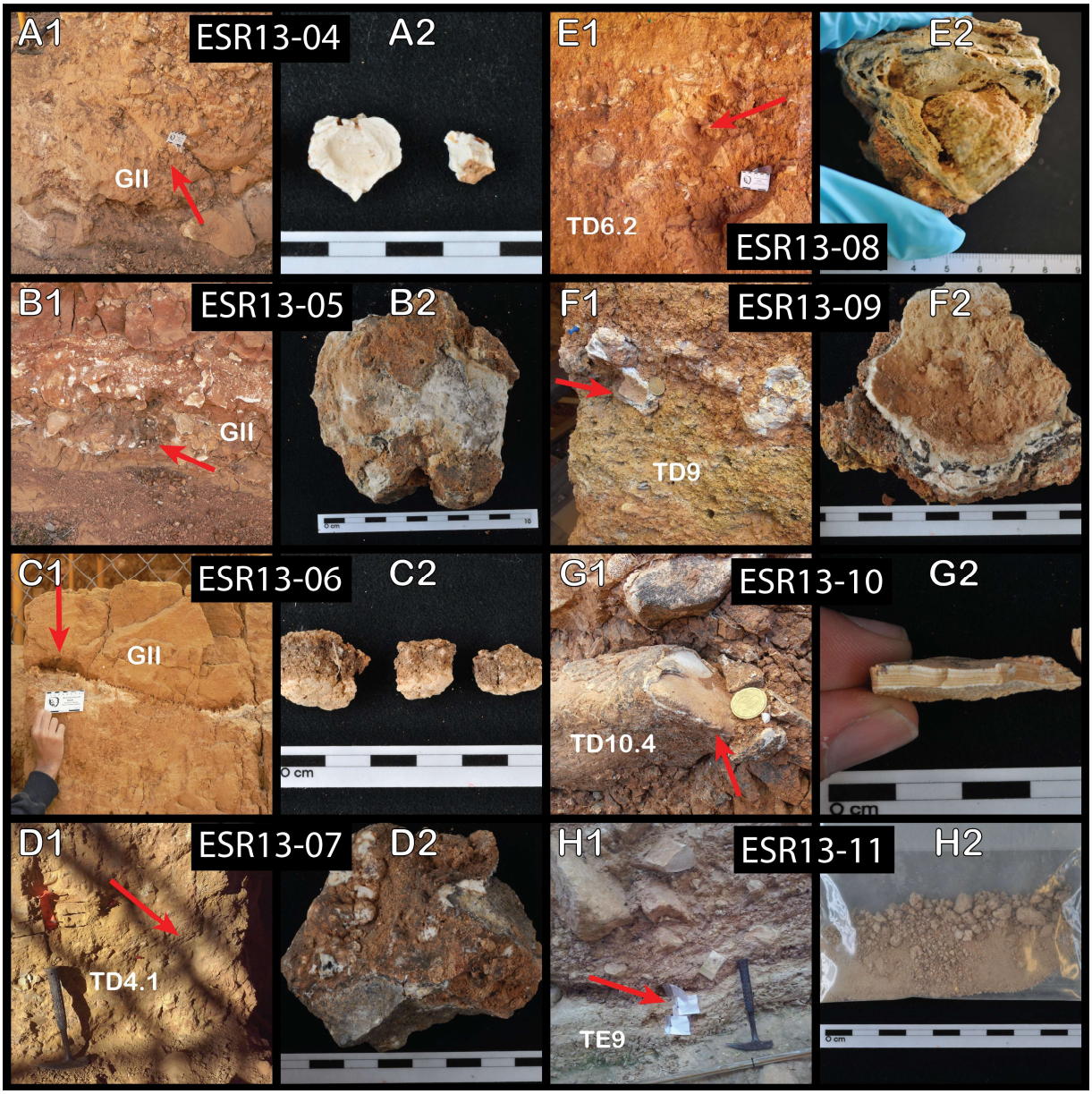
A1
ESR13-04
A2
GII
E1
E2
TD6.2
ESR13-08
B1
ESR13-05
B2
GII
F1
ESR13-09
F2
TD9
C1
ESR13-06
C2
GII
G1
ESR13-10
G2
TD10.4
D1
ESR13-07
D2
TD4.1
H1
ESR13-11
H2
TE9

Figure 4

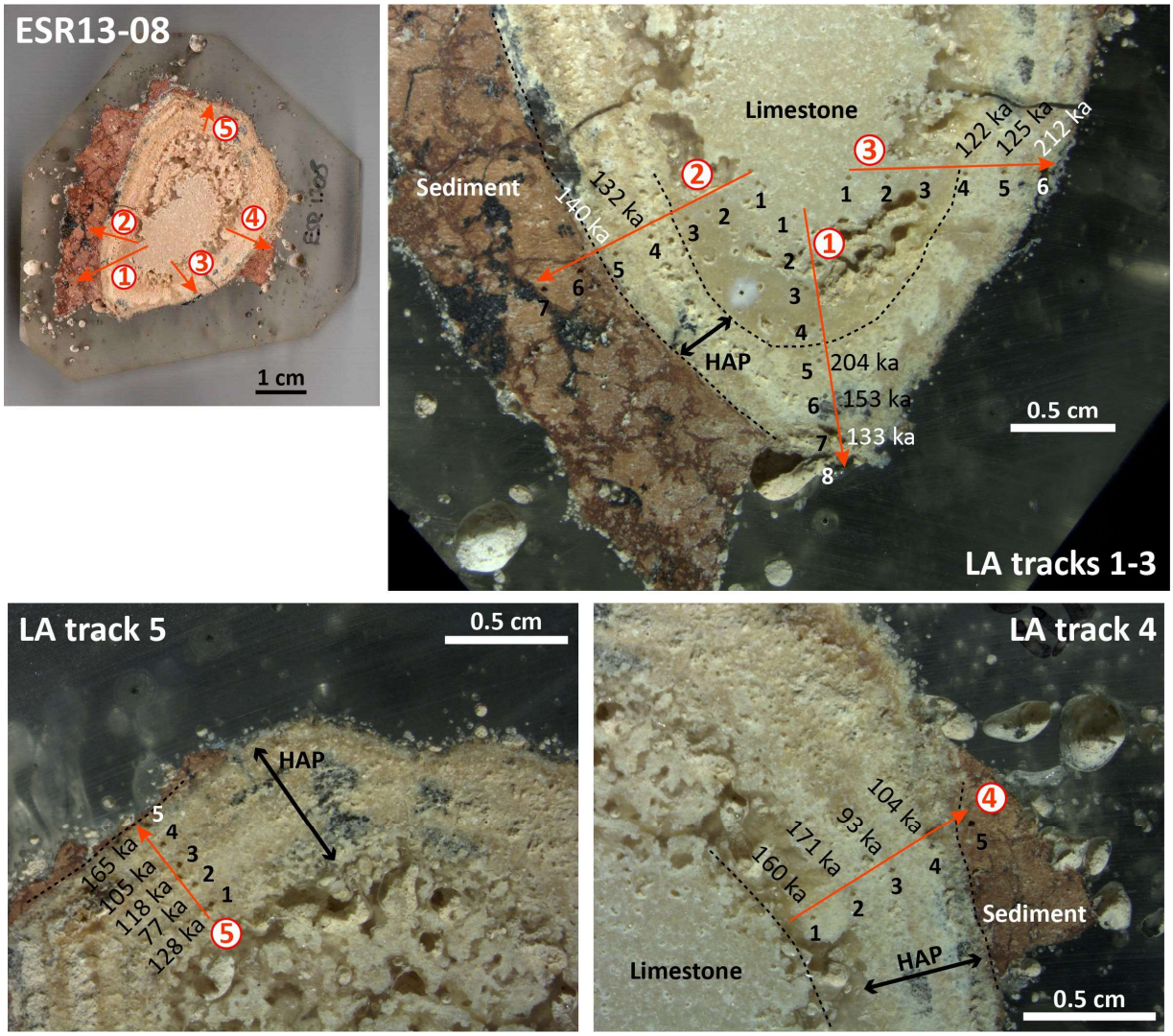
ESR13-08
1 cm
Limestone
Sediment
HAP
0.5 cm
LA tracks 1-3
LA track 5
LA track 4

Figure 5

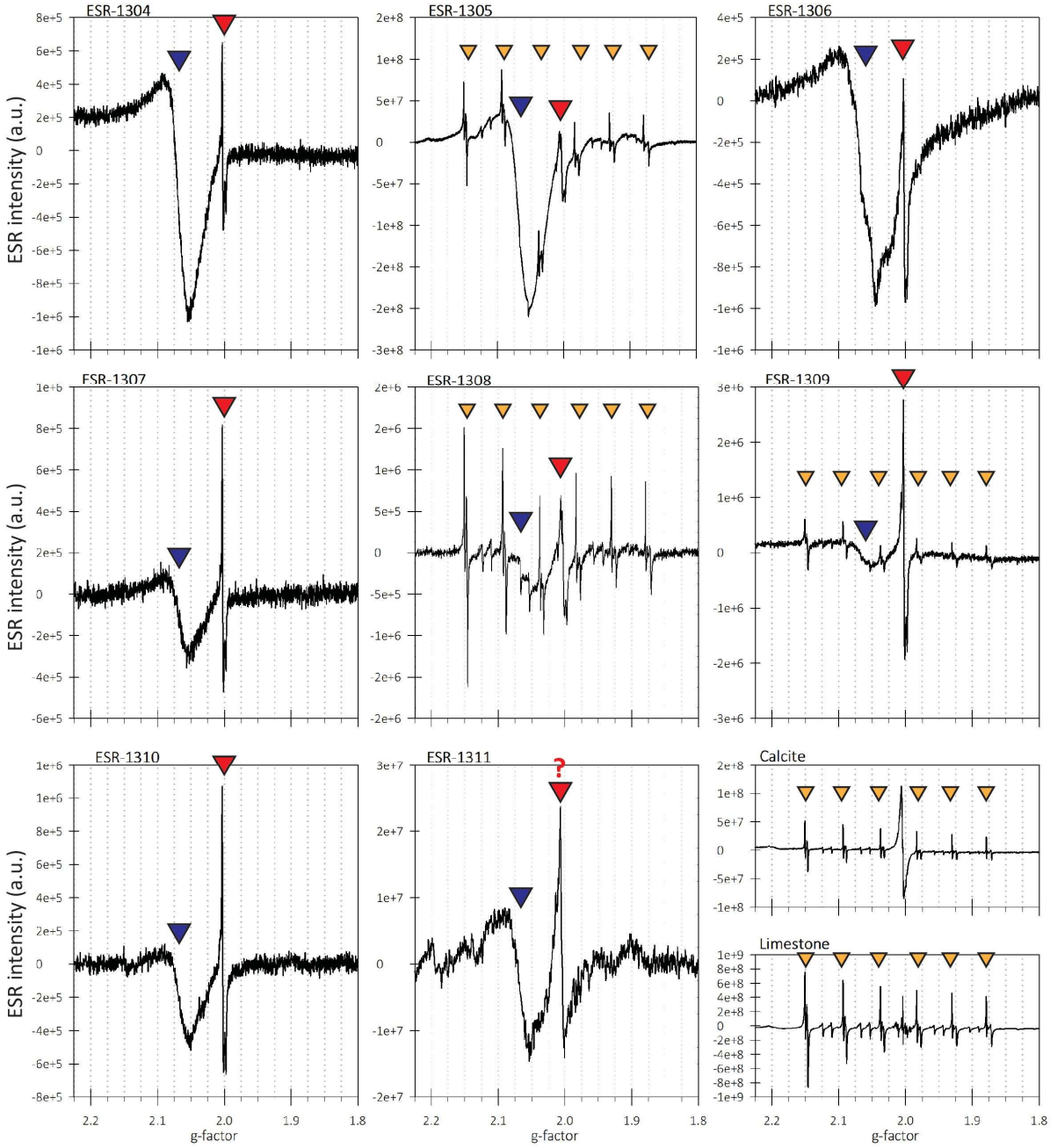
ESR-1304
ESR-1305
ESR-1306
ESR-1307
ESR-1308
ESR-1309
ESR-1310
ESR-1311
Calcite
Limestone
ESR intensity (a.u.)
g-factor
?

Figure 6

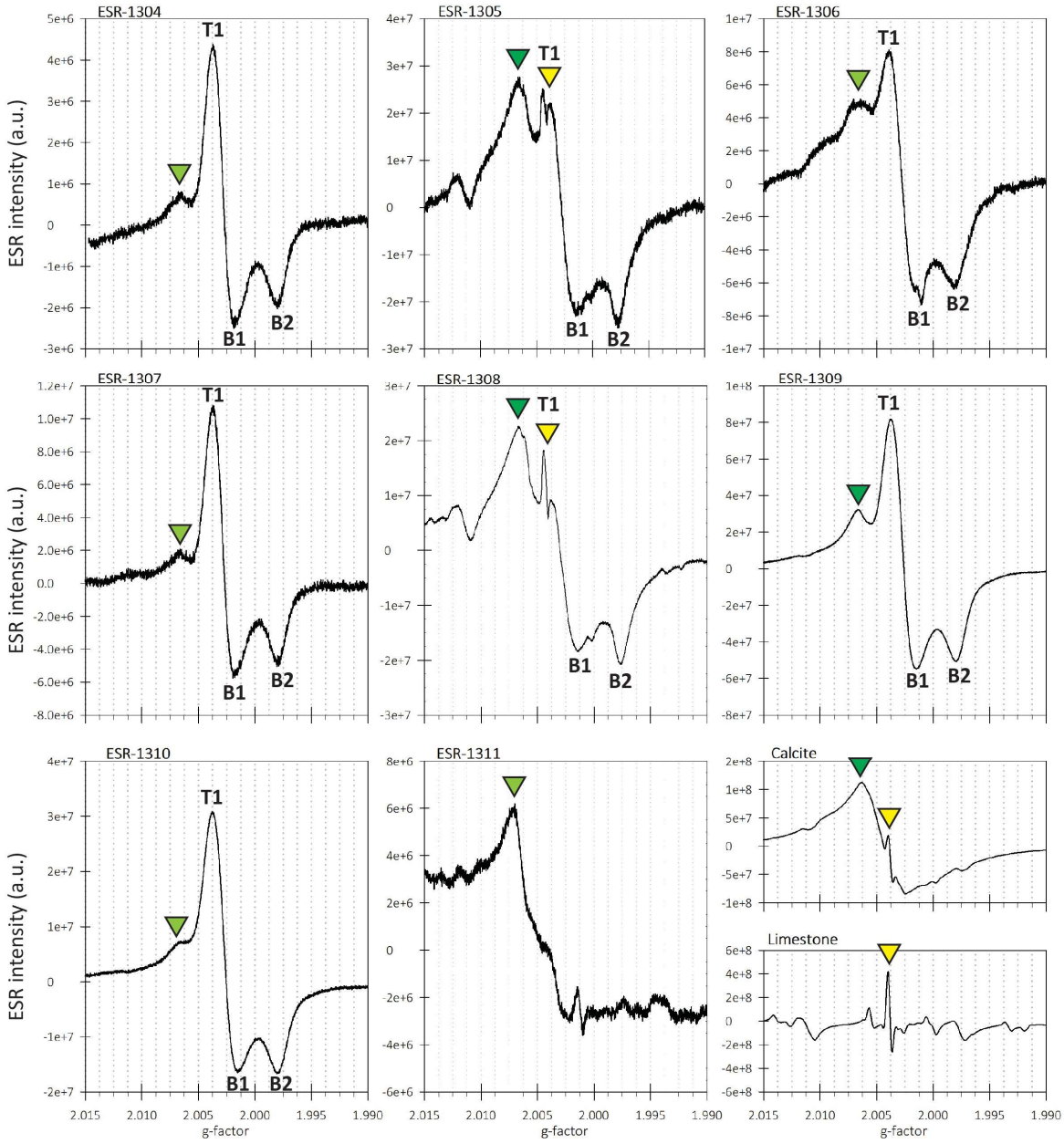
ESR-1304
ESR-1305
ESR-1306
ESR-1307
ESR-1308
ESR-1309
ESR-1310
ESR-1311
Calcite
Limestone
T1
B1
B2
ESR intensity (a.u.)
g-factor

Figure 7

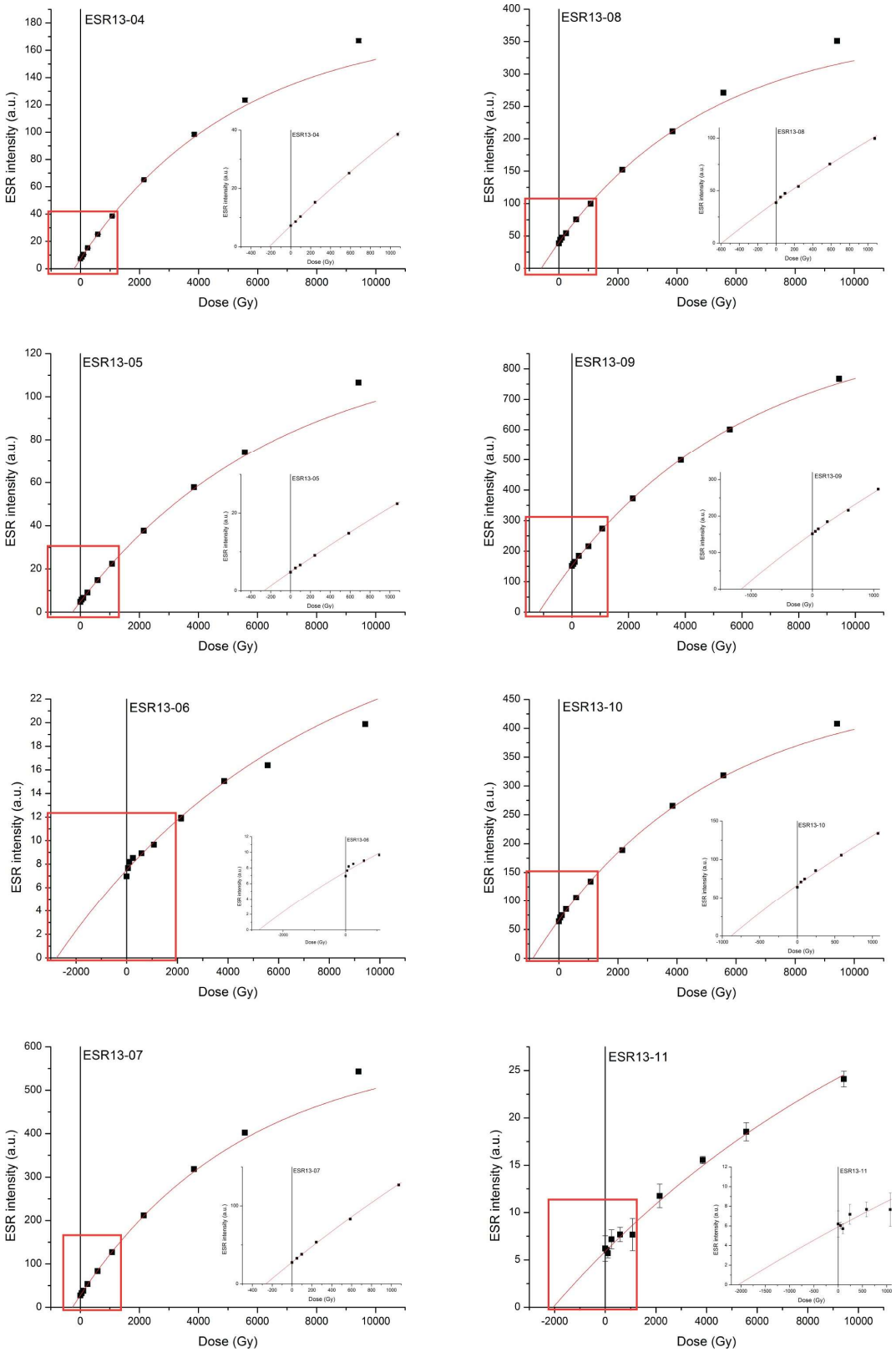
ESR13-04
ESR13-08
ESR13-05
ESR13-09
ESR13-06
ESR13-10
ESR13-07
ESR13-11
ESR intensity (a.u.)
Dose (Gy)